

1-1-2012

Residual Stresses in Suspension Plasma Sprayed Electrolytes in Metal-Supported solid Oxide Fuel Cell

Alpeshkumar Macwan
Ryerson University

Follow this and additional works at: <http://digitalcommons.ryerson.ca/dissertations>

 Part of the [Mechanical Engineering Commons](#)

Recommended Citation

Macwan, Alpeshkumar, "Residual Stresses in Suspension Plasma Sprayed Electrolytes in Metal-Supported solid Oxide Fuel Cell" (2012). *Theses and dissertations*. Paper 1245.

**RESIDUAL STRESSES IN SUSPENSION PLASMA SPRAYED ELECTROLYTES IN
METAL-SUPPORTED SOLID OXIDE FUEL CELL**

By

ALPESHKUMAR MACWAN

Bachelor of Engineering in Mechanical Engineering

Sardar Patel University (SPU)

Gujarat, India, 2003

A thesis

presented to Ryerson University

in partial fulfillment of the

requirements for the degree of

Master of Applied Science

in the program of

Mechanical Engineering

Toronto, Ontario, Canada, 2012

© Alpeshkumar Macwan 2012

AUTHOR'S DECLARATION

I hereby declare that I am the sole author of this thesis. This is a true copy of the thesis, including any required final revisions, as accepted by my examiners.

I authorize Ryerson University to lend this thesis to other institutions or individuals for the purpose of scholarly research.

I further authorize Ryerson University to reproduce this thesis by photocopying or by other means, in total or in part, at the request of other institutions or individuals for the purpose of scholarly research.

I understand that my thesis may be made electronically available to the public.

**RESIDUAL STRESSES IN SUSPENSION PLASMA SPRAYED ELECTROLYTES IN
METAL-SUPPORTED SOLID OXIDE FUEL CELL**

ALPESHKUMAR MACWAN

MASc., Mechanical Engineering

Ryerson University, Toronto, 2012

ABSTRACT

This study is aimed at identifying the change of residual stresses in suspension plasma sprayed (SPS) 8 mol% YSZ electrolytes on top of porous stainless steel substrate with varying processing parameters and temperatures. The residual stresses in the electrolyte layer are tensile with a value of approximately 90 MPa at room temperature. Porosity, microcracks and segmentation cracks are observed to form in the coating during post-deposition cooling. The decrease of residual stresses with increasing temperature is related to the changes in the Young's modulus, thermal expansion mismatch, micro-defects and possible creeping of porous stainless steel substrate. The coating fabricated using a torch power of 133 kW and stand-off distance of 90 mm exhibits the highest residual stress due to the formation of a denser microstructure and less cracking. Furthermore, the fracture toughness and interface fracture toughness of the SPS YSZ coating at the optimized condition was determined and discussed.

ACKNOWLEDGEMENTS

Several people should be acknowledged for their part in contributing to the work of this thesis. On the technical side of things, first is my supervisor: Dr. Daolun Chen, to whom I am of course forever grateful for his time, energy and guidance. I consider it a divine blessing to have met Dr. Chen, while I applied for Master of Engineering and was humbled by his agreement to take me as his student. In addition, I am forever indebted to Michael Marr and Dr. Olivera Kesler of University of Toronto, for providing plasma spray samples, and their support and discussion in completion of this work. I would like to thank Qiang Li, A. Machin, J. Amankrah and R. Churaman for their extraordinary cooperation in conducting the experiments. I would also like to extend my sincere thanks to all my friends and colleagues at Ryerson University.

I am grateful to Natural Sciences and Engineering Research Council of Canada (NSERC), Premier's Research Excellence Award (PREA), NSERC-Discovery Accelerator Supplement (DAS) Award, AUTO21 Network of Centers of Excellence, and Ryerson Research Chair (RRC) program for providing financial support.

Finally, while I offer everything, I do in life up to God, I dedicate this particular piece of work to four people: Ayana, my beautiful and loving daughter who changed my life, Sweta, who I cannot imagine myself without. She provided me with love, encouragement and support, without which this wouldn't be possible for me. Moreover, my parents, John and Pushpa Macwan, who are the rocks upon which all of my current and future success has been and will be built.

To

My Loving Daughter

Ayana

TABLE OF CONTENTS

AUTHOR’S DECLARATION.....	ii
ABSTRACT.....	iii
ACKNOWLEDGEMENTS.....	iv
TABLE OF CONTENTS.....	vi
LIST OF TABLES.....	ix
LIST OF FIGURES.....	x
NOMENCLATURE.....	xiii
Chapter 1: Introduction and motivation.....	1
1.1 Motivation for metal-supported SOFCs.....	2
1.2 Motivation for thesis work.....	4
1.3 Objective and scope of this thesis.....	6
Chapter 2: Background and previous work.....	8
2.1 Overview of SOFCs.....	8
2.1.1 SOFC history.....	8
2.1.2 SOFC principle.....	9
2.1.3 SOFC configurations.....	11
2.2 Materials for SOFCs.....	12
2.2.1 Electrolyte.....	13
2.2.2 Anode.....	13
2.2.3 Cathode.....	14

2.2.4	Metallic supports.....	14
2.3	Overview of plasma spray processes.....	15
2.3.1	Principle of plasma spray.....	15
2.3.2	Suspension plasma spraying (SPS).....	16
2.3.3	Process factors in the suspension plasma spray.....	17
2.4	Residual stresses.....	18
2.4.1	Quenching stress.....	19
2.4.2	Thermal mismatch stress.....	20
2.5	Reviews of residual stress measurement techniques.....	21
2.5.1	Residual stress measurements by X-ray diffraction method...	22
2.6	Fracture toughness using Vickers indentation technique.....	24
2.7	Interface fracture toughness.....	26
2.8	Recent studies on residual stresses in SOFC electrolyte coatings.....	28
Chapter 3: Experimental procedure.....		31
3.1	Suspension plasma spraying of YSZ electrolyte coatings.....	31
3.2	Residual stress measurement by X-ray diffraction.....	36
3.3	Microstructural analysis.....	40
3.4	Microhardness test.....	41
3.5	Fracture toughness using Vickers indentation technique.....	42
3.6	Interfacial indentation test.....	43
Chapter 4: Results and discussion.....		44
4.1	XRD characterization.....	44
4.2	Residual stresses.....	46

4.2.1	Surface roughness	46
4.2.2	X-ray diffraction and $\sin^2\psi$ measurements	47
4.2.3	Temperature dependent residual stress	51
4.3	Influence of torch power and stand-off distance.....	57
4.3.1	Effects on microstructure	57
4.3.2	Effects on residual stress	63
4.3.3	Effects on microhardness	66
4.4	Fracture toughness	68
4.4.1	Interface fracture toughness	69
Chapter 5: Conclusions and future work		72
5.1	Conclusions.....	72
5.2	Major contributions.....	75
5.3	Recommendations for the future work	76
References.....		79
Appendix.....		90

LIST OF TABLES

Table 2-1: Advantage and disadvantage of cell configurations.....	12
Table 2-2: Induced stresses in the coating during thermal spraying.....	21
Table 3-1: Suspension plasma spray parameters used to deposit the YSZ electrolyte coatings in the present study	33
Table 3-2: Parameters for plasma spray of LSM/YSZ cathode.....	34
Table 4-1: Residual stresses at different temperatures in the YSZ electrolyte fabricated with G2 spray condition (a torch power of 133 kW and a stand-off distance of 90 mm) along with the corresponding values of $E_{(531)}$ and $\nu_{(531)}$	56

LIST OF FIGURES

Fig. 2-1: General schematic of SOFC.....	10
Fig. 2-2: SOFC single cell configurations	11
Fig. 2-3: Schematic diagram of the suspension plasma spraying system.....	17
Fig. 2-4: Origin of quenching stress in plasma spray processing	20
Fig. 2-5: Strain measurement based on Bragg’s law	23
Fig. 2-6: Principle of interface indentation test and schematic representation of results	27
Fig. 3-1: (a) Mettech axial III plasma spray torch and (b) pressure vessel based suspension delivery system (University of Toronto).....	32
Fig. 3-2: A typical SEM image showing the cross-section of the SOFC half-cell, where the YSZ electrolyte was deposited with G2 spray condition (a torch power of 133 kW and a stand-off distance of 90 mm).....	35
Fig. 3-3: Typical cross-section SEM image of sample with MG 0.2 substrate, where YSZ electrolyte deposited with G2 spray condition.....	36
Fig. 3-4: Schematic diagram showing a coordinate system used to determine the strain using a high-temperature XRD	38
Fig. 3-5: Schematic view showing ψ tilt by iso-inclination (ω -rotation) or side-inclination (ψ -rotation)	38
Fig. 3-6: Panalytical X'Pert PRO MRD X-ray diffractometer.....	40
Fig. 3-7: The JSM-6380LV SEM system with EDS.....	41
Fig. 3-8: A Buehler Micromet-5100 Vickers microhardness tester.....	42
Fig. 4-1: XRD pattern of YSZ powder and SPS YSZ coating.....	45

Fig. 4-2: XRD pattern for the YSZ electrolyte of a metal-supported SOFC half-cell...	48
Fig. 4-3: XRD patterns showing the change of the (531) plane diffraction peak of the YSZ electrolyte with ψ at room temperature.....	49
Fig. 4-4: $\epsilon\text{-sin}^2\psi$ diagram for the (531) diffraction plane of the YSZ electrolyte determined at room temperature, where the solid line represents the linear least square fitting.....	50
Fig. 4-5: Residual stress in the YSZ electrolyte fabricated using process condition G2 (a torch power of 133 kW and a stand-off distance of 90 mm) as a function of temperature	51
Fig. 4-6: A higher magnification SEM cross-section image of SPS YSZ coating showing, A- macro porosity, B-micro porosity, C- un/partially melted particle, D- microcracks.....	53
Fig. 4-7: SEM cross-section image of SPS YSZ coating showing segmentation cracks	53
Fig. 4-8: SEM cross-section image of SPS YSZ coating after high temperature test ...	55
Fig. 4-9: SEM cross-section images of YSZ on LSM/YSZ + MG 2 substrate, (a) 100 kW, 90 mm (b) 133 kW, 90 mm (c) 133 kW, 120 mm (d) 133 kW, 70 mm (e) 162 kW, 90 mm	60
Fig. 4-10: SEM cross-section images of YSZ on MG 0.2 substrates, (a) 100 kW, 90 mm (b) 133 kW, 90 mm (c) 133 kW, 120 mm (d) 133 kW, 70 mm (e) 162 kW, 90 mm.....	62
Fig. 4-11: Residual stresses in the YSZ electrolyte layer at room temperature as a function of torch power at a constant stand-off distance of 90 mm	65
Fig. 4-12: Residual stresses in the YSZ electrolyte layer at room temperature as a	

function of stand-off distance with a constant torch power of 133 kW.....	65
Fig. 4-13: Hardness as a function of torch powers at a constant stand-off distance of 90mm.....	67
Fig. 4-14: Hardness as a function of stand-off distances at a constant torch power of 133 kW	67
Fig. 4-15: A typical SEM micrograph showing indentation crack propagation.....	69
Fig. 4-16: Typical SEM images showing interface indentation of YSZ coatings deposited on 430 porous stainless steel substrate at a load of (a) 50 g, (b) 100 g, and (c) 200 g	71

NOMENCLATURE

Acronym	Definition
CTE	Coefficients of thermal expansion
GHG	Greenhouse gas
GCO	Gd doped CeO ₂
LSM	lanthanum strontium manganite
LSGM	Lanthanum gallate
MG	Media grade
PEMFC	Proton exchange membrane fuel cell
ScSZ	Scandium doped zirconia
SDC	Samarium doped ceria
SEM	Scanning electron microscope
SLPM	Standard liter per minute
SOFC	Solid oxide fuel cell
SPS	Suspension plasma spraying
XRD	X-ray diffraction
YSZ	Yttria stabilized zirconia

<u>Symbol</u>	<u>Definition</u>	<u>Unit</u>
T_m	Melting temperature	K
ν	Poisson's ratio	
E	Young's modulus	GPa
α_c	Coefficient of thermal expansion of the coating	ppmK ⁻¹
T_c	Contact temperature between particle and the substrate	K
α_s	Coefficient of thermal expansion of the substrate	ppmK ⁻¹
ΔT	Temperature difference upon post deposition cooling	K
n	Integer for radiation wavelength	
λ	Radiation wavelength	Å
d	Inter planar spacing	μm
θ	Diffraction angle	deg
K_c	Fracture toughness of coating	MPam ^{1/2}
P	Peak load at indentation	N
c	Indentation crack length	μm
α	Empirical constant	
Z	Crack shape factor	
H	Coating hardness	GPa
σ_r	Residual stress in the coating	MPa
b	Crack depth	μm
K_{ca}	Interface fracture toughness	MPam ^{1/2}
P_c	Critical load during indentation	N
a_c	Critical crack length	μm

E_i	Young's modulus of interface material	GPa
H_i	Hardness of interface material	GPa
E_s	Substrate Young's modulus	GPa
H	Substrate hardness	GPa
$\sigma_1, \sigma_2, \sigma_3$	Principal stresses acting in the principal directions	MPa
\emptyset	Rotation angle around the sample normal	deg
ψ	Angle between the sample normal and the normal of the diffracting plane	deg
$\varepsilon_{\emptyset\psi}$	Strain measured in the direction of measurement	
σ_{\emptyset}	Single stress acting in a chosen direction	MPa
R_T	Coating roughness	μm
τ	X-ray penetration depth	μm
$E_{(531)}$	Young's modulus for the plane (531)	GPa
$\nu_{(531)}$	Poisson's ratio for the plane (531)	

Chapter 1: Introduction and Motivation

Today fuel cells are frequently reported in the news since they appear to be one of the most efficient and effective solutions to environmental problems that we face. Nowadays, 85% of the world's energy needs are met through the hydrocarbons (oil, coal, natural gas, and biofuels) oxidation, and this percentage is expected to remain above 82% for at least the next 30 years [1]. Over the same period, total world energy demand is projected to increase by 50% [1]. With their ability to operate on a range of fuels (hydrogen, methane, gasoline, diesel fuel, gasified coal, etc. [2,3], Solid Oxide Fuel Cells (SOFCs) present a unique opportunity to meet this demand in an environmentally responsible manner since they can increase the efficiency of the existing hydrocarbon-based infrastructure (with conversion efficiencies greater than 70% when utilized with co-generation) [3].

Extensive efforts to develop safe and reliable SOFCs for power generation and transportation applications are motivated by the pressing need for improved fuel efficiency, reduced anthropogenic greenhouse-gas emissions (GHG), and enhanced energy security [4-8]. This thesis represents a contribution to metal-supported SOFCs development effort in the way of further enhanced understanding of the structural characteristics and microstructural properties of YSZ (Yttria stabilized zirconia) electrolyte of metal-supported SOFCs. Specifically, this thesis focuses on microstructure and residual stress characterization of YSZ electrolyte and interpreting these results in the context of specific mechanisms of stress/microstructure evolution. Furthermore, the change of residual stress and microstructure with increasing temperature and with varying plasma spray process parameters is studied. The remainder of this chapter establishes the

motivation and framework for metal-supported SOFCs and the need for enhanced understanding of stress and microstructure of YSZ electrolyte material, followed by an overview.

1.1 Motivation for metal-supported SOFCs

In a general sense, fuel cells are devices that generate electricity by an electrochemical reaction of fuel and air. Different types of fuel cells exist and provide for a wide range of operating conditions and potential fuels, which have been documented in the literature [9,10]. SOFCs are a class of fuel cell devices utilizing a dense ceramic electrolyte capable of conducting gaseous ions, typically oxygen, at elevated temperatures ($\sim 600^{\circ}\text{C}$ or greater). This electrolyte is sandwiched between two porous electrode catalysts promoting the necessary reactions for the production of an electrical current.

One advantage of SOFCs over competing fuel cell systems is fuel versatility. Compared to competing fuel cell devices, such as proton exchange membrane fuel cells (PEMFC's) which are typically made of polymers that are poisoned by the presence of contaminants such as carbon monoxide, SOFCs require significantly less fuel processing and purification, allowing for a wider range of hydrocarbon fuels to be used, possibly eliminating the need for fuel processing completely through the introduction of steam with the fuel at the anode [10]. This steam is readily available from the overall reaction products because of the high-temperature operation. The integration of the hot gaseous exhaust of SOFCs with the turbine system allowed for overall fuel to electrical power conversion efficiencies of 57% with projected efficiencies with continued work approaching 75% [9,10].

In addition to the general performance advantages of SOFCs discussed above, there are several factors that make metal-supported SOFCs more attractive. One motivating factor for the metal-supported SOFCs is the intermediate operating temperature, which enables us to use relatively inexpensive stainless steel for both the electrical interconnects and mechanical support structures [11,12]. Also, the high electrical and thermal conductivity, superior toughness and thermal shock resistance, and good workability of metals are highly attractive attributes for SOFCs [13]. However, the incorporation of metallic materials in SOFCs requires intermediate operating temperatures to limit the occurrence of oxidation and prevent chromium evaporation in stainless steels, which could lead to possible cathode poisoning. Another motivating factor for the use of metal-supported SOFCs is potential for redox stability and shorter start-up time compared to the conventional anode-supported SOFCs. There is also a possibility of improved electrochemical performance through the use of thinner electrolyte layer. Thinner electrolytes (as well as thinner anode and cathode layers) decrease the internal electrical/ohmic resistance of the fuel cell stack, thus improving net power output. Perhaps more important, however, is the potential for improved ionic conductivity with reduced thickness or, alternatively, the potential for maintaining adequate ionic conductivity and reducing the operating temperature of the fuel cell. This possibility was explored by Steele, who proposed that the typical operating temperature of the most common electrolyte material (YSZ) may be reduced from $\sim 800\text{-}1000^\circ\text{C}$ down to $\sim 600^\circ\text{C}$ using electrolyte thickness on the order of $\sim 1\mu\text{m}$ [14-16].

These potential advantages of SOFCs in various power applications have been noted by several others attempting to develop metal-supported SOFC materials and devices [11,17-19]. These

efforts have been successful in demonstrating power density of 0.26 Wcm^{-2} at 600°C and 0.56 Wcm^{-2} at 700°C with dry hydrogen as fuel [18].

1.2 Motivation for thesis work

A key technical barrier that limits the widespread commercialization and application of SOFCs is their high operating temperature, which leads to high material cost and reduces performance and, ultimately, the durability and lifetime [6,20,21]. One approach to reduce the cost is to lower the operating temperature to an intermediate range ($650\text{-}800^\circ\text{C}$), which enables the use of relatively inexpensive stainless steel for both the electrical interconnects and mechanical support structures [11,12]. Metal-supported SOFCs have recently received considerable attention [17-19,22].

When fabricating conventional anode-supported SOFCs, the electrolyte and electrode functional layers are typically deposited as wet ceramic powder slurries, which are then solidified by sintering at high temperatures. It is difficult to apply these wet ceramic fabrication methods to the metal-supported SOFCs because the high temperature sintering commonly required to densify the electrolyte could rapidly oxidize or densify porous stainless steel supports. Therefore, an alternative direct deposition fabrication method such as plasma spraying could facilitate the fabrication of metal-supported SOFCs. In the plasma spraying, feedstock powders are melted and accelerated by a plasma jet towards a substrate. Upon impact on the substrate, the molten particles flatten and solidify to form “splats”, which accumulate to form coating layers [23,24]. This process readily permits the deposition of ceramic coatings on metallic supports without additional post-deposition heat treatment. As a rapid deposition process, plasma spraying could

reduce manufacturing costs, especially at low and intermediate volumes compared to more time-consuming wet ceramic methods. Suspension plasma spraying (SPS) is a modification of the traditional plasma spray process in which the feedstock powders are suspended in liquid for feeding to the plasma rather than fed as dry, flowable powders with the use of carrier gas. The suspension permits the use of smaller feedstock powders as well, so that SPS could potentially be used to produce thinner coating layers and more refined microstructural features [25].

A challenging issue in the fabrication of plasma sprayed coatings lies in the presence of residual stresses that originate from splat quenching and from the difference in the thermal expansion between the coating and substrate materials after cooling down to room temperature from the deposition temperature. These stresses can lead to coating cracking, which reduces the cell performance and can lead to catastrophic failure of the cell, especially if it occurs in the electrolyte. The formation of cracks in a coating typically relieves the residual stresses, to some extent. Therefore, understanding the residual stress using different process conditions can provide useful insight into the mechanical integrity of the coating layers prior to electro-chemical fuel cell testing. Furthermore, since the metal-supported SOFCs are operated at temperatures ranging from 650-800°C, it is also important to ascertain the residual stress in this temperature range and especially its change with temperature due to the thermal cycling during SOFC operation. While some residual stress values at room and elevated temperatures in YSZ electrolytes in anode-supported or cathode-supported planar SOFCs fabricated by other processes have been reported [26-28], to the authors' knowledge, no studies on the residual stresses of metal-supported planar SOFCs made by plasma spraying have been reported in the literature. These observations and requirements motivate the work presented in this thesis.

1.3 Objective and scope of this thesis

The general objective of this thesis is to experimentally characterize the microstructure, residual stresses and mechanical properties of electrolyte for metal-supported SOFCs. As mentioned earlier, the generic SOFC device architecture is that of an electrolyte membrane sandwich between two porous electrodes anode and cathode. This porosity may significantly reduce the structural integrity of the anode and cathode layers. Therefore, to first order, the properties of the electrolyte layer will control the mechanical response of the SOFC membrane structure. This thesis is focused predominantly on investigating residual stress, microstructure and mechanical properties of the most likely electrolyte materials of SPS 8 mol% YSZ. Generally, YSZ has been a focus in our research because it is the most common electrolyte material (in large part due to cost and availability). Furthermore, the YSZ deposition process was a recently developed suspension plasma spray process, capable of producing dense and gas-tight electrolyte layer without post-deposition heat treatment. Previous studies indicated the presence of residual stress in plasma sprayed YSZ as a major contributing factor to the stability and durability of SOFCs [26-28]. It is well known that the residual stress state of thin film is inherently linked to the microstructure of the material. Therefore, the main objectives of this thesis are:

- ✓ To characterize as-deposited residual stress in SPS YSZ electrolyte and its variation with increasing temperature.
- ✓ To study the variation of residual stress, microstructure and hardness with varying process parameters, e.g., torch power and stand-off distance.

- ✓ To determine the fracture toughness and interface fracture toughness of SPS YSZ electrolyte coatings.

The approach taken for meeting these goals is mostly experimental. Considering the need for a broader range of information in the development of metal-supported SOFCs, the experimental approach focused on gaining insights using some available advanced testing method and apparatus. In the chapter 2, the necessary background about SOFCs, material system, plasma spray and stress evolution in plasma sprayed YSZ coating is established. This is followed by chapter 3, which describes experimental procedures used the characterization of stress and results and discussion presented in the chapter 4.

Chapter 2: Background and Previous Work

2.1 Overview of SOFCs

Today fuel cells are reported a lot in the news since they appear to be one of the most efficient and effective solutions to environmental problems that we face nowadays. Despite their modern high-tech aura, fuel cells actually have been known in science for more than 160 years and have become the subject of intense research and development, especially since World War II. Out of different types of fuel cells, SOFCs have recently emerged as a serious high-temperature fuel cell technology. They are promising to be extremely useful in large, high-power applications such as full scale industrial stations, large-scale electricity-generating stations and motor vehicles [29].

2.1.1 SOFC history

In the late 1930s, Emil Baur, a Swiss scientist and his colleague H. Preis experimented with solid oxide electrolytes using such materials as zirconium, yttrium, cerium, lanthanum, and tungsten oxide. The operation of the first ceramic fuel cell at 1000°C, by Baur and Preis, was achieved in 1937 [30]. In the 1940s, O.K. Davtyan of Russia added monazite sand to a mix of sodium carbonate, tungsten trioxide, and soda glass, to increase the conductivity and mechanical strength. Davtyan's design, however, also experienced unwanted chemical reactions and short life ratings. The Central Technical Institute in the Hague, Netherlands, Consolidation Coal Company, in Pennsylvania, and General Electric, in Schenectady, New York Research accelerated research into solid oxide technology by 1950s. A 1959 discussion of fuel cells noted

that problems with solid electrolytes included relatively high internal electrical resistance, melting, and short-circuiting, due to semiconductivity. The promise of a high temperature cell that would be tolerant of carbon monoxide and use a stable solid electrolyte continued to draw modest attention. In 1962, researchers at Westinghouse, for example, experimented with a cell using zirconium oxide and calcium oxide. More recently, climbing energy prices and advances in materials technology have invigorated the research on SOFCs. The fuel cell of 220 kW built by Siemens Westinghouse, and the micro turbine by Northern Research and Engineering Corporation is running on natural gas and achieving an efficiency of 60% in a year of actual operating conditions. Furthermore, a world record for SOFC operation, roughly eight years, still stands, and the prototype cells have demonstrated two critical successes: the ability to withstand more than 100 thermal cycles, and voltage degradation of less than 0.1% per thousand hrs.. Moreover, a 140 kW peak powered SOFC cogeneration system, supplied by Siemens Westinghouse, is presently operating in the Netherlands. This system has operated for over 16,600 hrs., becoming the longest running fuel cell in the world [29].

2.1.2 SOFC principle

SOFCs are an energy conversion device that produces electricity by electrochemically combining a fuel and an oxidant across an ionic conducting oxide electrolyte. Figure 2-1 shows the general schematic of SOFCs, where the dense electrolyte is sandwiched between two porous electrodes, the anode and the cathode (the anode/electrolyte/cathode sandwich is referred to as a single cell). Fuel is fed to the anode, undergoes an oxidation reaction, and releases electrons to the external circuit. Oxidant is fed to the cathode, accepts electrons from the external circuit, and

undergoes a reduction reaction. The electron flow in the external circuit from the anode to the cathode produces direct-current electricity. In an SOFC stack, single cells are connected in electrical series via a component called the interconnect [31]. An SOFC single cell can be configured into various shapes depending on the specific stack design. SOFC cells have been made into tubular, flat-plate or planar, bell-and-spigot, banded, and corrugated structures [31,32]. The tubular concept is far more advanced, whereas the planar design offers higher volumetric and gravimetric power density, concerning long-term stability and demonstration of plant technology.

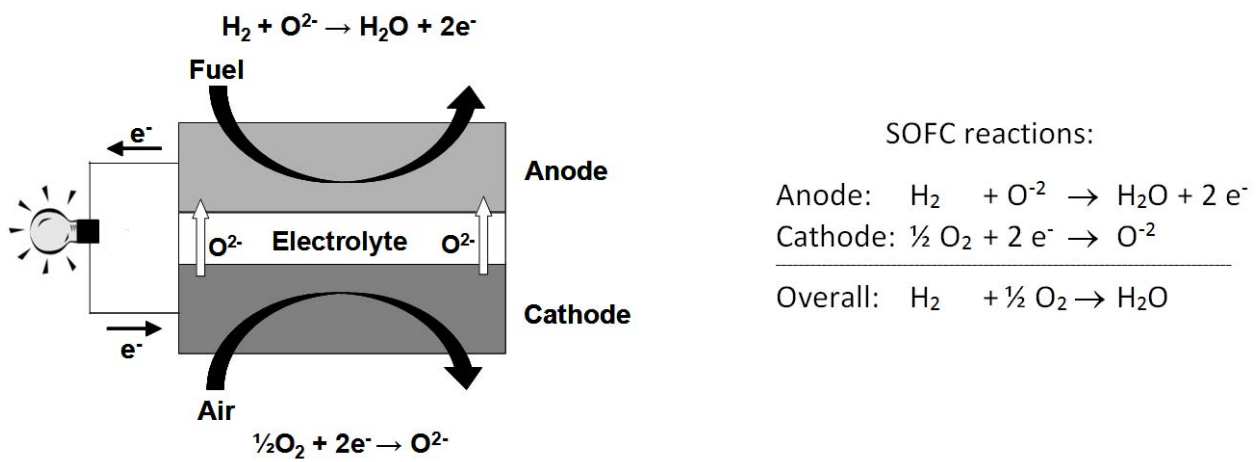


Fig. 2-1: General schematic of SOFC [33].

2.1.3 SOFC configurations

The configurations in SOFC single cells can be classified into two broad categories: self-supporting and external-supporting. In the self-supporting configuration, one of the cell components (often the thickest layer) acts as the cell structural support. Thus, single cells can be designed as electrolyte-supported, anode-supported, or cathode-supported. In the external-supporting configuration, the single cell is configured as thin layers on the interconnect or a porous substrate. The various cell configurations for SOFCs are schematically shown in Figure 2-2. The advantage and disadvantage of each cell configuration are listed in Table 2-1.

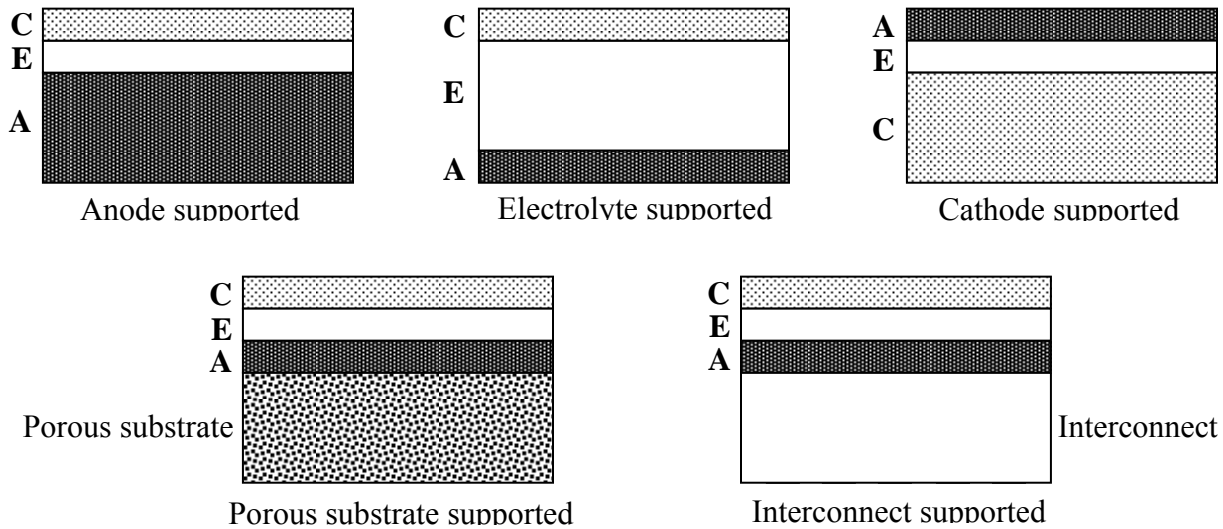


Fig. 2-2: SOFC single cell configurations [31].

Table 2-1: Advantage and disadvantage of cell configurations [10].

Cell configuration	Advantage	Disadvantage
<i>Self-supporting</i>		
Electrolyte-supported	Relatively strong structural support from the dense electrolyte Less susceptible to failure due to anode reoxidation (Ni/YSZ anode) and cathode reduction (LSM cathode)	Higher resistance due to low electrolyte conductivity Higher operating temperatures required to minimize electrolyte ohmic losses
Anode-supported	Highly conductive anode Lower operating temperature via use of thin electrolytes	Potential anode reoxidation Mass transport limitation due to thick anodes
Cathode-supported	No oxidation issues but potential cathode reduction Lower operating temperature via use of thin electrolyte	Lower conductivity Mass transport limitation due to thick cathodes
<i>External-supporting</i>		
Interconnect-supported	Thin cell components for lower operating temperature Stronger structures from metallic interconnects	Interconnect oxidation Flow field design limitation due to cell support requirement
Porous substrate	Thin cell components for lower operating temperature Potential for use of non-cell material for support to improve properties	Increased complexity due to addition of new materials Potential electrical shorts with porous metallic substrate due to an uneven surface.

2.2 Materials for SOFCs

The SOFC is a multilayer structure consisting of ceramic and metallic materials. There are different types of SOFC concepts, basically tubular and planar ones, which differ in the single cell design and arrangement, interconnector materials and gas flow. SOFC materials have to fulfill different requirements.

2.2.1 Electrolyte

In a SOFC, electrolyte resistance is predominant in the resistance of the entire cell. To improve the cell performance of the flat-plate type, the resistance of the electrolyte should be reduced. There are two approaches to this improvement: to use a material of higher electrical conductivity or to reduce the thickness of the electrolyte by improving the mechanical strength. YSZ is most widely used as the electrolyte, because of its high oxide ion and low electronic conductivity, and stability under reducing and oxidizing atmospheres [34]. However, there are other materials such as Gd doped CeO₂ (GCO), Lanthanum gallate (LSGM), scandium doped zirconia (ScSZ), and samarium doped ceria (SDC) are also possible electrolyte candidates for SOFCs.

2.2.2 Anode

Anodes in SOFCs are charged with the task of electro-oxidation of hydrocarbon fuels. That is, oxygen ions must react with the hydrocarbon to generate water and carbon dioxide and release electrons. To achieve high fuel cell efficiency, one must not only identify highly active anode materials, but also ensure the anode surface area to be adequately high to provide a great concentration of reaction sites. Anode material requires being highly electroconductive, sufficiently electrocatalytic, porous enough for efficient gas transportation, and thermal expansion compatible with other cell components. Considering cost and performance, the Ni/YSZ cermet materials are still the most common anode for SOFCs [35].

2.2.3 Cathode

To increase the cell performance at decreased operating temperatures, the polarization losses of the electrodes, mainly the cathode has to be decreased. The electrochemical properties of the cathode can be influenced by choosing an appropriate composition. Lots of perovskite types as well as other oxides have been investigated with respect to their suitability as a cathode material. Lanthanum strontium manganite (LSM)/YSZ composite is commonly used as a cathode material due to its high electrical and oxide ion conductivity.

2.2.4 Metallic supports

Metal-supported SOFCs have been recognized as a promising alternative to conventional cermet or ceramic-supported SOFCs. The metal-supported, such as stainless steel supported SOFCs exhibit high mechanical strength, good ductility, and matching thermal expansion coefficient with Zirconia and Ceria-based electrolytes. Structural limitations arise not only from the thermal stress at rapid start-up and during temperature fluctuations, but also from the mechanical stress from assembly compaction and vibrations. Therefore, metal-supported SOFCs fulfil the requirements of structural robustness and thermal shock resistance with low internal temperature and stress gradients. Stainless steels are available commercially in a wide range of compositions and microstructures. The unit price of steel is at least one order of magnitude lower than the ceramic components such as NiO and YSZ. Thus, the total material cost can be reduced significantly. Metallic substrates can be easily fabricated into desired shapes, such as planar, circular tubular and flat tubular by traditional machining at low cost. The use of metallic

substrates allows the use of conventional metal joining and forming techniques, and could significantly reduce the manufacturing costs of SOFC stacks as well.

2.3 Overview of plasma spray processes

2.3.1 Principle of plasma spray

Plasma spraying, first developed in the 1960s, is a well-established manufacturing technique to produce value-added coatings to enhance wear resistance, temperature resistance, and to repair parts [36]. In the plasma spraying, feedstock powders are melted and accelerated by a plasma jet towards a substrate. Upon impact on the substrate, the molten particles flatten and solidify to form “splats”, which accumulate to form coating layers [23,24]. The technique utilizes plasma created by high-voltage electrodes to melt particles that traverse the plasma jet and are deposited on a substrate [37]. Anode nozzle exit velocities are typically on the order of 900-2000 ms⁻¹ [38,39]. Plasma jet temperatures generally vary between 7000 K and 20,000 K [40]. Consequently, all known inorganic materials can be deposited, as the melting temperatures T_m of all materials lie below the plasma jet temperature. Low deposition efficiencies can result from high vaporization rates of the deposited materials, from the material rebound, which occurs when the particles have only partially melted or resolidified prior to impact, or from the parameters of the deposition. The deposition efficiency decreases with an increase in plume spread or with rotation of a planar sample holder. The spraying distance and the jet velocity affect the residence time in the plasma, which determines whether the materials have been sufficiently melted before reaching the substrate, or are already resolidified, leading to partially/unmelted particles. Cooling

rates greatly depend on the substrate heat conduction and surface topography, and lie in the range of $106,000 \text{ Ks}^{-1}$ to $107,000 \text{ Ks}^{-1}$, similar to the rates achieved in liquid quenching [40,41]. Coatings are formed by the consecutive buildup of impacting coating material splats [42]. The conventional powder plasma spraying use spray feedstock powders typically between 10 and 100 μm in diameter due to the requirement of flowing the powders in a carrier gas, and therefore, produces porous and thick layers. Due to low-cost and flexibility of plasma spraying, several research efforts have been devoted towards the development of plasma spraying processes to synthesise dense and thin YSZ layers with improved mechanical properties and performance for their use as SOFC electrolyte.

2.3.2 Suspension plasma spraying (SPS)

Recently, suspension plasma spraying (SPS), a modification of the traditional plasma spray process has been developed [17,25,43,44]. It uses feedstock powders suspended in a carrier liquid for feeding to the plasma rather than fed as dry, flowable powder with the use of carrier gas. Figure 2-3 shows the schematic diagram of the suspension plasma spraying system. In this process, a feed suspension is injected directly into the plasma flame. The plasma liquid interaction atomizes the suspension into a fine mist and evaporates the suspension medium, thereby concentrating the solid content into micro-sized particles [45,46]. The small particles are nearly immediately accelerated to the plasma gas velocity. At impact on the substrate, the particles form thin lamellae at rapid solidification rates. With a lower solid content of the suspensions, more electrolyte particles are completely melted, and a denser coating can be deposited. By adjustment of the process conditions, SPS can potentially produce dense thinner

film layers, and more refined microstructural features leading to improved properties [17,25]. Such a deposition process emerged as a good candidate for manufacturing thinner and dense electrolyte for SOFCs.

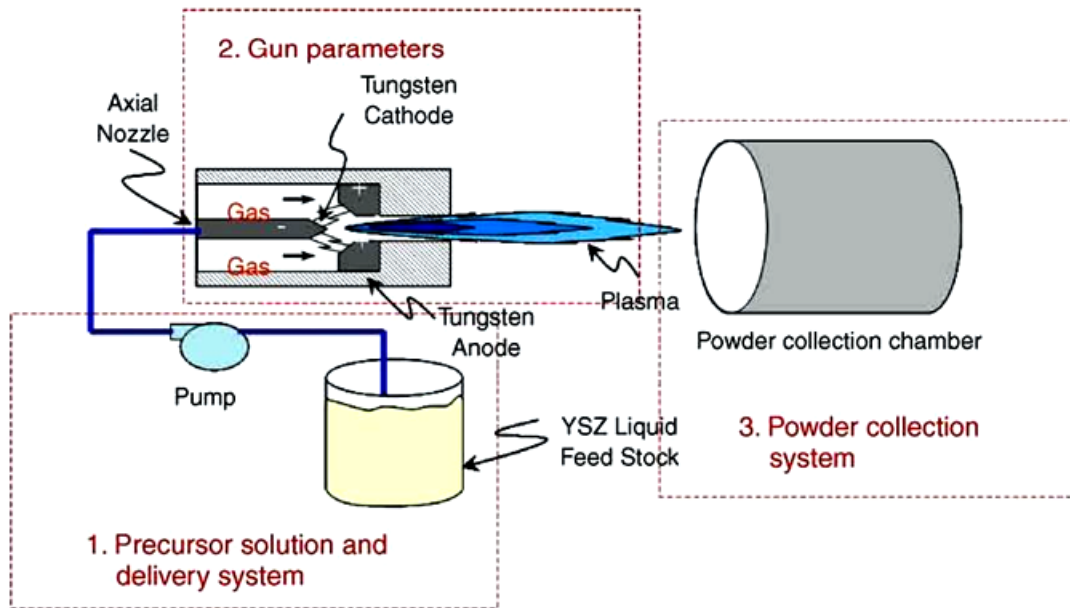


Fig. 2-3: Schematic diagram of the suspension plasma spraying system [47].

2.3.3 Process factors in the suspension plasma spray

The plasma spray process parameters greatly influence the microstructure and properties of the sprayed coating. There are numerous intrinsic and extrinsic plasma spray parameters, which require a highly sophisticated system to control them. The most common control parameters are [48],

- ✓ Power input,
- ✓ Arc gas pressure,

- ✓ Auxiliary gas pressure (helium, hydrogen, nitrogen),
- ✓ Powder gas pressure,
- ✓ Powder feed rate
- ✓ Grain size/shape,
- ✓ Injection angle (orthogonal, downstream, upstream),
- ✓ Surface roughness,
- ✓ Substrate heating,
- ✓ Spray distance
- ✓ Spray divergence and
- ✓ Spray atmosphere.

A variety of secondary parameters that are associated with the above parameters are also important for achieving good-quality plasma spray coatings. These secondary parameters include quench rate, residence time of particles in jet, gas composition of plasma jet, heat content, etc.

2.4 Residual stresses

One of the characteristics in a plasma spray coating is the presence of the residual stress. Large temperature differences experienced during the thermal spray processing lead to residual stresses in the component, and they strongly affect its performance and durability. In service, the applied stress is superimposed on the residual stress which may either add up or reduce each other depending on their respective sign, with consequential effects on failure. Therefore, it is important to understand the stress state before the SOFC component enters the service, and

modify the spraying process through a better understanding of the stress development so as to identify a favorable condition. Residual stresses can be sub-divided into two main contributions: (i) quenching stress or primary stress, and (ii) thermal mismatch stress or secondary stress.

2.4.1 Quenching stress

As shown in Figure 2-4, the quenching stress arises as individual splats rapidly solidify and cool from a molten state to the substrate temperature, while their contraction is restricted by adhesion to the substrate. These quenching stresses are always tensile. Quenching stress becomes independent of the substrate material and its surface pre-treatment as long as the coating thickness exceeds approximately 10 μm [49]. Thereafter, the steady-state value of quenching stress is a function of the characteristics of the impinging particles and the substrate temperature only [49]. The quenching stress could be expressed as [50],

$$\sigma_q = \frac{E_c}{1 - \nu_c} \alpha_c (T_m - T_c), \quad (2.1)$$

where ν_c and E_c are the Poisson ratio and Young's modulus of the coating, α_c is co-efficient of thermal expansion of the coating, T_m is melting temperature of particles and T_c is contact temperature between particle and the substrate.

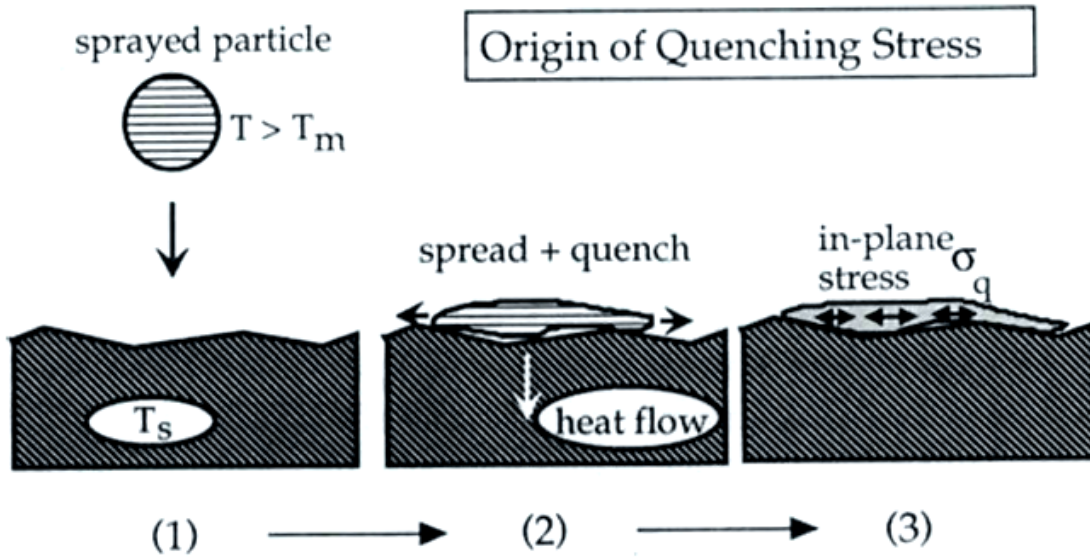


Fig. 2-4: Origin of quenching stress in plasma spray processing [49].

2.4.2 Thermal mismatch stress

Thermal mismatch stress or secondary stress is caused by the difference in the thermal expansion coefficients between the coating (α_c) and substrate (α_s), which leads to residual stresses induced by the mismatch of thermal shrinkage during cooling from the process temperature (average temperature reached by the coating-substrate system after deposition) to room temperature, during the so-called secondary cooling. Depending on the sign of this difference and the deposition temperature, the evolution of thermal stresses could be in a tensile or compressive nature [51].

The thermal mismatch stress could be expressed as [52],

$$\sigma_t = \frac{E_c}{1-\nu_c} (\alpha_c - \alpha_s) \Delta T, \quad (2.2)$$

where ν and E are the Poisson ratio and Young's modulus of the coating, α_c is co-efficient of thermal expansion of the coating, α_s is co-efficient of thermal expansion of the substrate, ΔT is the temperature difference upon post deposition cooling with respect to room temperature.

The resulting overall residual stress depends on the magnitude of quenching and thermal mismatch stress as shown in Table 2-2.

Table 2-2: Induced stresses in the coating during thermal spraying [53].

Origin of stresses	Resulting stresses for different relationships between α_c and α_s		
	$\alpha_c < \alpha_s$	$\alpha_c = \alpha_s$	$\alpha_c > \alpha_s$
Quenching stress	+	+	+
Thermal mismatch stress	-	0	+
Resulting overall residual stress	+ or -	+	+

+ → tensile stress; - → compressive stress.

2.5 Reviews of residual stress measurement techniques

There are several commonly used methods of stress determination in thin film coatings, which include mathematical modeling (analytical or numerical), material removal techniques (hole drilling, layer removal), mechanical methods (curvature, displacement, or strain measurement) and diffraction (X-ray or neutron) methods. Each technique has certain advantages and limitations; their applicability is determined by such factors as shape, dimensions, materials of the coating and the substrate, knowledge of the constituents' properties and processing conditions, and also the availability of the necessary equipment [51]. The work presented in this

thesis focuses on the residual stress determined via an X-ray diffraction technique. The important aspects of this technique are presented below.

2.5.1 Residual stress measurements by X-ray diffraction method

One of the most widely used residual stress measurement techniques is based on X-ray diffraction. X-ray stress analysis is derived from two fundamental theories: the theory of elasticity, which defines the relationship between stresses and strains, and X-ray diffraction theory, which give the relationship between the atomic arrangement in a solid and its diffraction pattern. The Bragg law is the basis of stress analysis by X-ray diffraction. Figure 2-5 illustrates the relationship between strain and diffraction angle. The gray spots represent the atomic positions in a strain-free crystal. The light horizontal lines represent the crystal planes in the strain-free crystal. For the strain-free crystal, the Bragg law is given by,

$$n\lambda = 2d \sin \theta , \quad (2.3)$$

where n is an integer for a radiation wavelength of λ , d is inter planer spacing and θ is half of a diffraction angle.

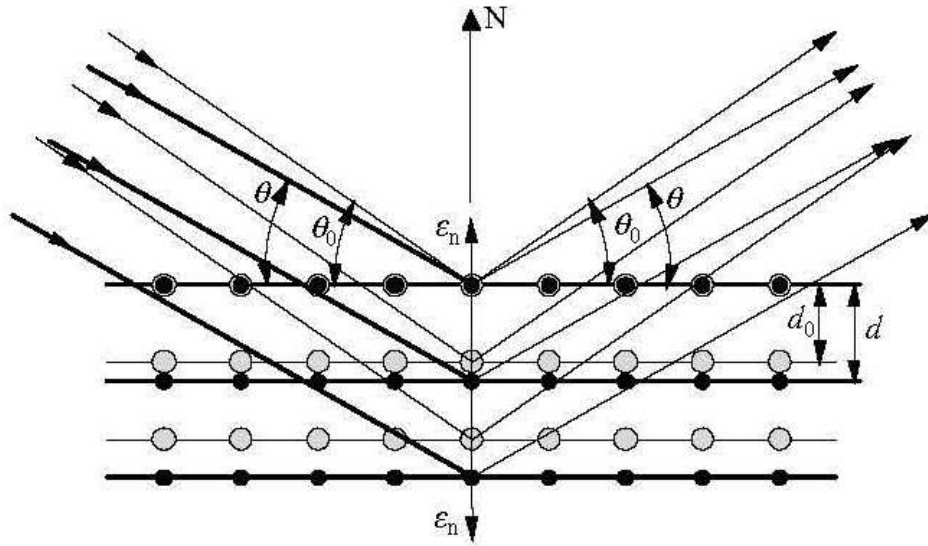


Fig. 2-5: Strain measurement based on Bragg's law [54].

It has been shown that there is a clear relationship between the diffraction pattern that is observed when X-rays are diffracted through crystal lattices and the distance between atomic planes (the inter-planar spacing) within the material. By altering the inter-planar spacing different diffraction patterns will be obtained. Changing the wavelength of the X-ray beam will also result in a different diffraction pattern. The inter-planar spacing of a material that is free from strain will produce a characteristic diffraction pattern for that material. When a material is strained, elongations and contractions are produced within the crystal lattice, which change the inter-planar spacing of the $\{hkl\}$ planes. This induces a change in d , which in turn causes a shift in the diffraction pattern. By a precise measurement of this shift, the change in the inter-planar spacing can be evaluated and thus the strain within the material can be obtained. To do this, it is necessary to establish mathematical relationships between the inter-planar spacing and the strain.

In order to measure a single acting stress σ_ϕ in a chosen direction, i.e., at an angle θ to σ_1 , elasticity theory for an isotropic solid show that the strain along an inclined line is,

$$\varepsilon_{\phi\psi} = \frac{1+\nu}{E} \sigma_\phi \sin^2 \psi - \frac{\nu}{E} (\sigma_1 + \sigma_2), \quad (2.4)$$

where ν and E are the Poisson ratio and Young's modulus of the coating, σ_1 and σ_2 are principal stresses parallel to sample surface [54]. It is important to point out that Eq. (2.4) is particularly valid for thin-film samples. In most cases it could be assumed that the stresses in the through-thickness direction are negligible and that the stresses are the same in all directions within the plane of the coating. Eq. (2.4) forms the basis of the $\sin^2\psi$ method. It suggests that a plot of strain $\varepsilon_{\phi\psi}$ versus $\sin^2\psi$ yield a straight line whose slope is represented by $\sigma_\phi (1+\nu)/E$, therefore,

$$\sigma_\phi = \frac{E}{1+\nu} m, \quad (2.5)$$

where m is the slope of $\varepsilon_{\phi\psi}$ versus $\sin^2\psi$ curve. This is the basis of stress determination using X-ray diffraction.

2.6 Fracture toughness using Vickers indentation technique

Toughness is one of the important mechanical properties of a material. The term toughness refers to the ability of a material to absorb energy during deformation up to fracture, usually measured in terms of fracture toughness [55]. Measurement of fracture toughness for bulk materials is classical, and is done routinely in research and development (R&D) or production using, for example, the Charpy tests, four-point or three-point bending tests, compact tension tests, etc. [56,57]. However, these methods can barely apply for a thin film due to the size limitation of the film thickness. For hard coatings bonded to substrates, researchers make use of nanoindentation

on coatings or bending of ductile substrates to generate different types of coating cracking, based on which various methods for fracture toughness measurements are proposed.

The Vickers indentation technique has been considered a simple and attractive method for assessing the toughness of ceramic materials because of the ease and low cost of conducting experiments. The method uses Vickers microhardness indenter to induce radial cracks in the coating. The principle of this method is based on the ability of coatings to inhibit crack propagation. The relationship between fracture toughness and crack length was established decades ago [58],

$$K_c = \alpha \left(\frac{E}{H} \right)^{1/2} \frac{P}{c^{3/2}}, \quad (2.6)$$

where P is peak load at indentation, c is crack length, and α is an empirical constant which depends on the geometry of the indenter, $\alpha=0.016$ for both a Berkovich and Vickers type indenter. The derivation of Eq. (2.6) assumes an “unlimited” sample thickness. In practice, the application of Eq. (2.6) requires that the depth b of the half-penny crack beneath the surface be less than one-tenth of the thickness of the sample [59]. During the coating fabrication process, residual stresses are generated in the coating. These residual stresses affect the crack propagation behavior and subsequently the fracture toughness of the coating. The fracture toughness for coating with residual stresses can be calculated using the following equation [55],

$$K_c = \alpha \left(\frac{E}{H} \right)^{1/2} \frac{P}{c^{3/2}} + Z\sigma_r c^{1/2}, \quad (2.7)$$

where Z is crack shape factor given by [55]

$$Z = 1.12\sqrt{\pi} \frac{b/c}{\left(\frac{3\pi}{8}\right) + \left(\frac{\pi}{8}\right)(b/c)^2}, \quad (2.8)$$

$Z=1.26$ for an idealized half-penny, i.e., the depth b of the crack is equal to the crack length c , making the half-penny an ideal semicircle. To meet the geometrical requirements of Eqs. (2.6) or (2.7), the indentation depth (smaller than the depth b of the crack induced) should be much less than 10% of the coating thickness.

2.7 Interface fracture toughness

One of the important characteristics of the coating is the reliability of the bond between the coating and the substrate. During the past decade, it was proposed to use the interfacial indentation test as an alternative to other tests in order to characterize the adhesive properties of thermal spray coatings [60,61]. This test consists of measuring the length of cracks generated at the coating-substrate interface as a consequence of Vickers indentations performed at the interface using varying applied loads. Figure 2-6 shows the principle of interface indentation technique. In a bilogarithmic coordinate, the relationship between the crack radius and the applied load is linear and allows a critical load (P_c) under which no crack is generated at the interface to be defined.

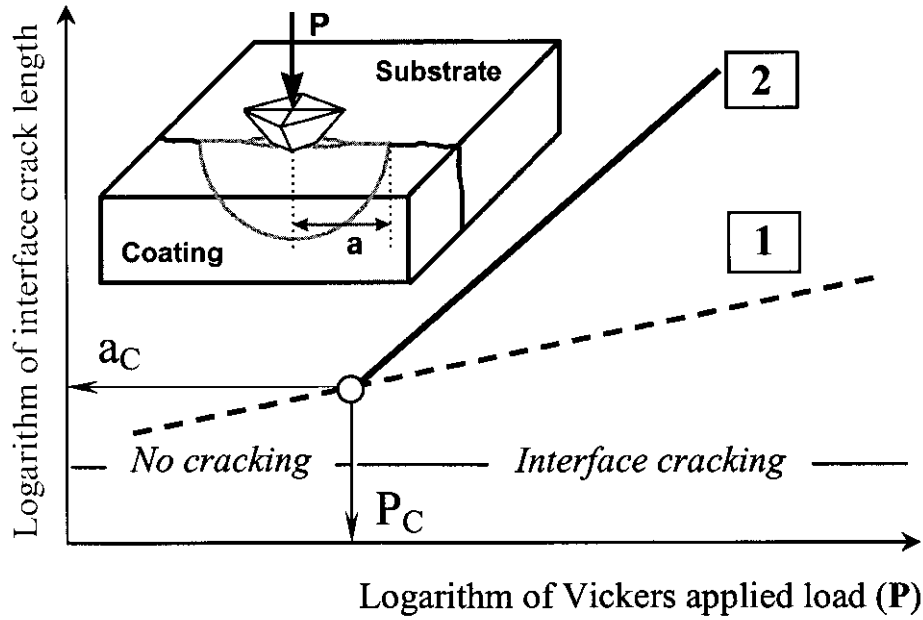


Fig. 2-6: Principle of interface indentation test and schematic representation of results [62].

The adhesion between the coating and the substrate is defined by the following equation [62],

$$K_{ca} = 0.015 \left(\frac{E}{H}_i \right)^{1/2} \frac{P_c}{a_c^{3/2}}, \quad (2.9)$$

where K_{ca} is the interfacial indentation toughness, P_c is the critical load, and a_c is the corresponding indentation diagonal measured in the plane of the interface. E_i is Young's modulus, and H_i is the Vickers hardness of the interface material. This type of relation is only valid for cracks that are longer than the radius of the plastic zone. When a crack is formed, its propagation is aided by the flexion of the coating due to the action of the indenter which plays the role of a wedge inserted at the interface between the coating and the substrate. It should be noted that the propagation will depend on the coating thickness since, a thicker coating will resist the flexion much better than a thinner one. As a consequence, the slope of the crack line will be affected by the elastic behavior of the coating. The only point of the cracking line which is not

concerned with this phenomenon is the crack initiation point P_C . This is the basis for selecting critical load and the critical crack length [62].

During indentation, a plastic deformation zone is created by sharing the combined local properties of the coating and the substrate. Eventually, a local crack may be likely to occur in the interface plane if the fracture toughness of this composite interface material is attained. The purpose of the interface indentation test is to give a quantitative measure of the apparent fracture toughness.

At the interface, the factor $\left(\frac{E}{H}\right)_i^{1/2}$ in equation (2.9) can be expressed as [62],

$$\left(\frac{E}{H}\right)_i^{1/2} = \frac{(E/H)_s^{1/2}}{1+(H_s/H_c)^{1/2}} + \frac{(E/H)_c^{1/2}}{1+(H_c/H_s)^{1/2}}, \quad (2.10)$$

and the subscripts i, s and c stand for interface, substrate and coating, respectively.

2.8 Recent studies on residual stresses in SOFC electrolyte coatings

SOFCs are receiving more attention in the research due to their various advantages as mentioned earlier. There has been a lot of studies to characterize residual stress, microstructure, mechanical properties and its variation with temperature and process parameters [17,25-28]. A brief background related to the previous studies on SOFC properties is described in the following section.

Fischer *et al.* [26] studied in-plane residual stress distribution in the electrolyte of an anode-supported planar SOFCs using XRD method. The materials for electrolyte, anode and cathode were 8YSZ, Nio/8YSZ and LSM/YSZ+LSM, respectively. The electrolyte and anode functional layer was manufactured using vacuum slurry coating. The measured residual stress was -560 MPa at room temperature for an approximately 10 μm thick electrolyte layer on an oxidized ~ 1.5 mm thick anode substrate. Chemical reduction of the anode leads to a slight decrease of the electrolyte stress to -520 MPa. At an operation temperature of 800°C the stress is lower by a factor of about two, but still remains compressive.

Huang and Harter [28] also studied room temperature residual stress in the electrolyte of a cathode-supported planar SOFCs using XRD method. The study was carried out with bi-layer structure consisting of 8YSZ electrolyte and Ca-doped LaMnO_3 cathode substrate fabricated by Siemens plasma spray technology. The Siemens plasma spray technology includes plasma spraying of electrolyte followed by co-densification at 1345°C for 6h. The result revealed that the residual stress at room temperature is -60 MPa and remains unchanged up to a temperature of 600°C. Further increase in temperature to 1000°C results in a decrease in the residual stress but remains still under compression. The decrease of compressive residual stress with increasing temperature was related to the lattice relaxation and creep deformation of substrate.

Malzbender *et al.* [27] studied residual stress at room temperature and high temperature (1000°C) using XRD and curvature method in the electrolyte of an anode-supported planar SOFC. The room temperature residual stress was -600 MPa and decreased with increasing temperature. At 900°C, the compressive residual stress was almost negligible. Similarly, the

curvature of half-cell strips diminished as a function of temperature. Moreover, changes in the electrolyte residual stress associated with cell brazing to steel interconnects were measured. After joining, the stress in the probing electrolyte increased by about -45 MPa.

Yakabe *et al.* [63] evaluated the residual stresses in the electrolyte of anode-supported planar SOFCs experimentally and numerically. The materials for electrolyte and anode were 8YSZ and NiO/YSZ, respectively. Both the electrolyte and anode were fabricated by screen printing followed by co-firing at 1500°C. The estimated residual stress in the electrolyte was around -650 MPa. It was observed that the residual stress was larger at the center part of the cell. They also studied the effects of the cell geometry, the flattening treatment, the fabrication method of the electrolyte, and the reduction of the anode on the residual stress.

To summarize the above studies available in the literature, it can be concluded that the residual stresses present in SOFCs depend on many factors including the type of manufacturing process, processing parameters, post-deposition treatment, compatibility between materials of electrolytes, electrodes and supports and cell configurations. Also, the thermal gradient developed during thermal cycling has a major effect on the residual stresses. However, no studies on the residual stresses in the electrolyte of metal-supported planar SOFCs made with SPS process have been seen in the literature. The objective of the present study is, therefore, to identify the change of residual stresses with temperature in the YSZ electrolyte layers of porous 430 stainless steel-supported planar SOFCs produced by plasma spraying with varying plasma spray parameters, including torch power and stand-off distance.

Chapter 3: Experimental Procedure

3.1 Suspension plasma spraying of YSZ electrolyte coatings

All YSZ electrolyte coatings were deposited by suspension plasma spraying with an Axial III DC torch (Northwest Mettech Corp., North Vancouver, BC, Canada). Figure 3-1 shows Mettech Axial III plasma spray torch and pressure vessel based suspension delivery system. The Axial III produces three plasma streams that converge within the torch before exiting through a nozzle as a single jet. Suspensions are injected axially into the convergence zone of the plasma streams. Five different spray conditions, shown in Table 3-1, were selected. For five different conditions, the plasma torch input power for spray conditions G4, G2 & G5 was 100 kW, 133 kW and 162 kW, respectively, with a constant stand-off distance of 90 mm. The stand-off distance for spray conditions G1, G2 & G3 was 70 mm, 90 mm and 120 mm, respectively, with a constant torch power of 133 kW. In each condition, the electrolytes were deposited on two different substrates LSM/YSZ + MG 2 and MG 0.2. Where MG indicates the media grade (MG), the maximum particle size, in μm , that should be able to pass through the filter pore structure. For example, MG 2 indicates that pores are sized to filter out particles with diameters larger than 2 μm . The targeted thickness for all coatings was 50 μm , but the thickness of individual coatings ranged from approximately 45 to 51 μm , except for the coating fabricated using G3 spray condition, which had a thickness of approximately 71 μm . The coating made with a spray condition of G2 (Table 3-1) on LSM/YSZ + MG 2 substrate, which had a torch power of 133 kW and a stand-off distance of 90 mm, was selected to determine the residual stress as a function of temperature up to 750°C, while the residual stresses in the electrolyte coatings made with all five spray

conditions were measured at room temperature. The samples very received from University of Toronto.

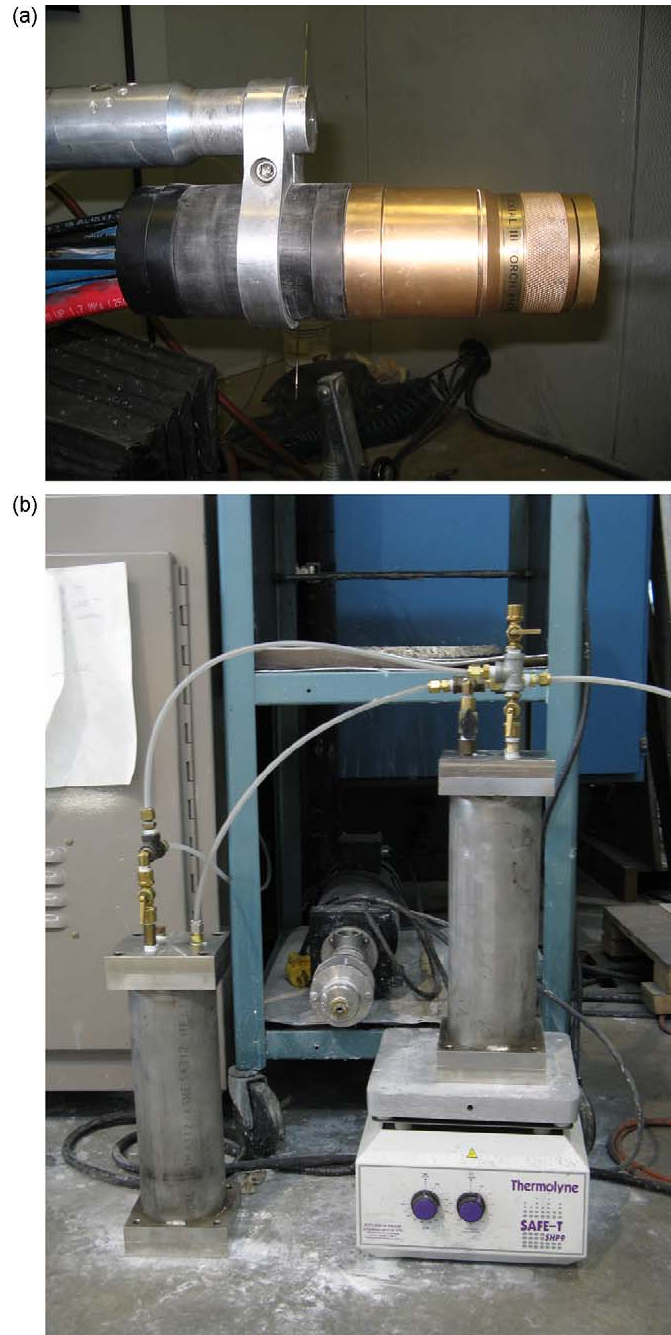


Fig. 3-1: (a) Mettech axial III plasma spray torch and (b) pressure vessel based suspension delivery system (University of Toronto).

Table 3-1: Suspension plasma spray parameters used to deposit the YSZ electrolyte coatings in the present study.

Identifier	G1	G2*	G3	G4	G5
Torch power, kW	133	133	133	100	162
Stand-off distance, mm	70	90	120	90	90
Plasma gas flow rate, slpm	275	275	275	275	275
Ar (%)	30	30	30	74	25
N ₂ (%)	65	65	65	21	70
H ₂ (%)	5	5	5	5	5
Current, A	600	600	600	600	750
Nozzle, mm	9.5 (3/8")	9.5 (3/8")	9.5 (3/8")	9.5 (3/8")	9.5 (3/8")
Substrate	LSM/YSZ + MG 2 / MG 0.2				

* Indicates the coating condition used to fabricate the YSZ electrolyte in which the temperature-dependent residual stress is measured.

The feedstock suspensions were made with 8 mol% YSZ (Y_{0.15}Zr_{0.85}O_{1.925}) powder (Inframat Advanced Materials, Manchester, CT) dispersed in deionized water at a solid loading of 3 vol. %. The powder had a d_{50} of approximately 2.6 μm . Polyethyleneimine was added as a dispersant to enhance stability [44]. The suspension was fed to the torch at 21 ml min⁻¹ with a peristaltic pump-based feeding system (Northwest Mettech Corp.) and injected into the plasma through a syringe tube with a 0.84 mm inner diameter. To enhance the atomization of the suspension, 30 slpm N₂ was fed around the outside of the syringe tube. The torch was mounted to a robot that rastered across the substrates at 635 mm s⁻¹ in horizontal stripes separated by vertical steps of 3.78 mm.

The electrolytes were deposited on cathode layers, which were previously deposited on metallic supports. The cathodes consisted of about 40 μm thick composite layers of LSM and YSZ, which is a typical SOFC cathode composite material. A mixture of 48.2 wt% LSM and 51.8 wt% 8mol% YSZ powders (Inframat Advanced Materials, Farmington, CT, USA) was used for the cathode layers. Spray dried cathode powders were sieved and mechanically mixed before plasma spraying. The detailed powder preparation procedure has been reported previously [50] and the powder size range is given in Table 3-2.

Table 3-2: Parameters for plasma spray of LSM/YSZ cathode [50].

Parameters	Cathode
Feedstock	48.2 wt% LSM/51.8 wt% YSZ powder
Particle size, μm	-45+32 / -32+25
Plasma gas flow rate, slpm	250
Plasma gas composition	23.3% N ₂ , 76.7% Ar
Torch current (A per cathode)	183
Nozzle size, mm	9.5
Number of passes	60
Preheat temperature, °C	300
Stand-off distance, mm	100

The metallic supports were porous 430 stainless steel discs (Mott Corp., Farmington, CT) having a diameter of 25.4 mm and a thickness of approximately 1.6 mm. These discs are typically used as filters and are designated by media grade (MG).

The electrolyte-cathode-support structure is often referred to as SOFC “half-cell”. A typical SEM image of a cross-section of a half-cell is shown in Fig. 3-2, where the upper YSZ

electrolyte, the intermediate LSM/YSZ cathode, and the lower porous 430 stainless steel substrate layers are indicated.

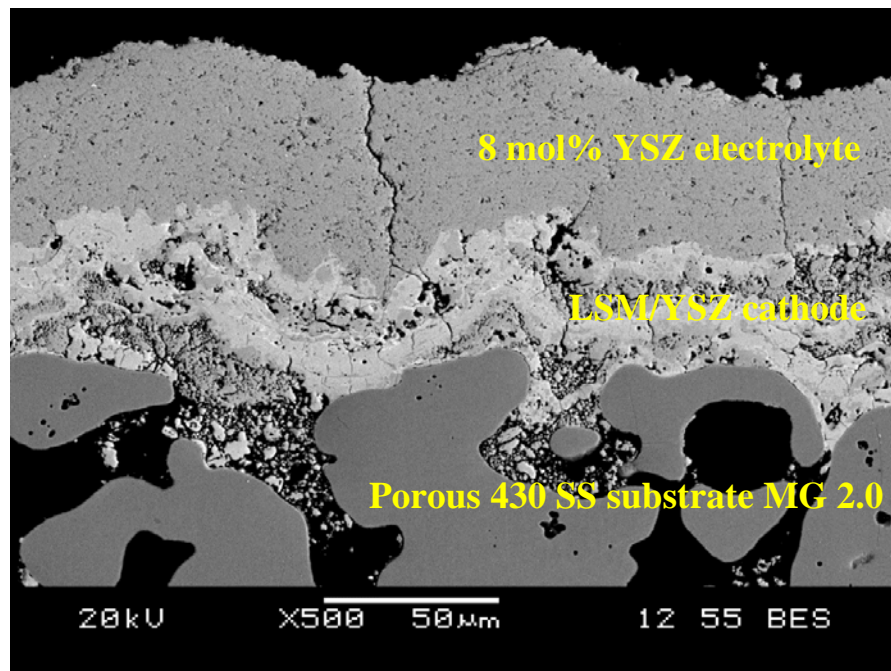


Fig. 3-2: A typical SEM image showing the cross-section of the SOFC half-cell, where the YSZ electrolyte was deposited with G2 spray condition (a torch power of 133 kW and a stand-off distance of 90 mm).

A typical cross-section SEM image with MG 0.2 substrate is shown in Fig. 3-3, where the upper YSZ electrolyte and the lower porous 430 stainless steel substrate layers are indicated.

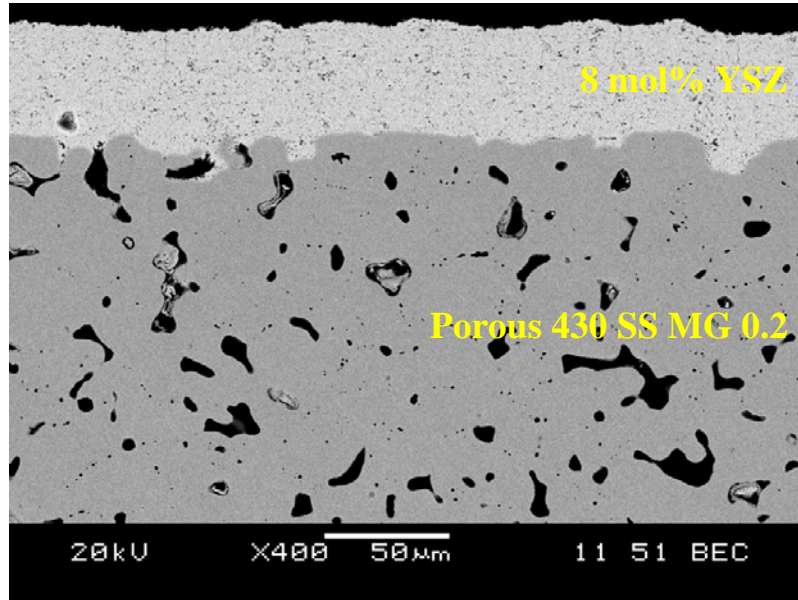


Fig. 3-3: Typical cross-section SEM image of sample with MG 0.2 substrate, where YSZ electrolyte deposited with G2 spray condition.

3.2 Residual stress measurement by X-ray diffraction

Among the various methods available for residual stress measurements, X-ray diffraction (XRD) is a powerful method due to its non-destructive nature. It could also be used to distinguish stresses in different phases. Therefore, the residual stresses in the YSZ electrolyte were determined at room temperature and high temperatures using a high-temperature, high resolution X-ray diffractometer. In measuring the residual stress using XRD, the strain in the crystal lattice is determined from the change in the interplanar spacing d , and the associated residual stress is determined using the elastic constants (Young's modulus E and Poisson's ratio ν) of the coating

material, assuming a linear elastic distortion of the crystal lattice planes. Figure 3-4 shows a sample coordinate system used for the strain determination, where $\sigma_1, \sigma_2, \sigma_3$ are principal stresses acting in the principal directions, θ is the rotational angle around the sample normal, ψ is the angle between the sample normal and the normal of the diffracting plane, $\varepsilon_{\theta\psi}$ is the strain measured in the direction of measurement defined by the angles θ and ψ , and σ_{θ} is the single stress acting in a chosen direction, i.e., at an angle θ to σ_1 . It was assumed that $\sigma_3=0$ because the measurement was made from the surface or in the coating thickness direction. The commonly-used $\sin^2\psi$ method has been adopted for the residual stress measurement in the present study. The configuration for the diffraction measurement and stress analysis is schematically shown in Fig. 3-5, where the three sample rotation angles ω, θ and ψ are indicated. The measurement of residual stresses with the $\sin^2\psi$ method requires at least ψ tilt [54]. This ψ tilt can be achieved by ω rotation (iso-inclination) or ψ rotation (side-inclination) as shown in Fig. 3-5. In this study the side-inclination method (ψ -method) is used, then the sample normal (S_3) is out of the diffractometer plane (a plane containing X-ray incident beam and diffracted beam) for all non-zero ψ tilt angles.

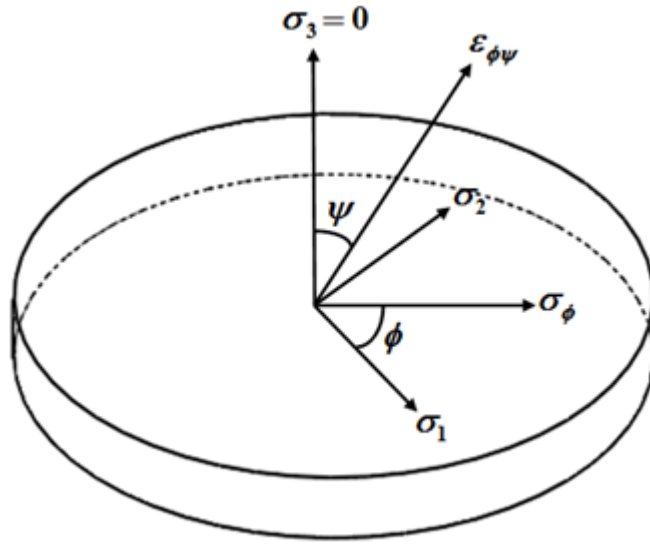


Fig. 3-4: Schematic diagram showing a coordinate system used to determine the strain using a high-temperature XRD.

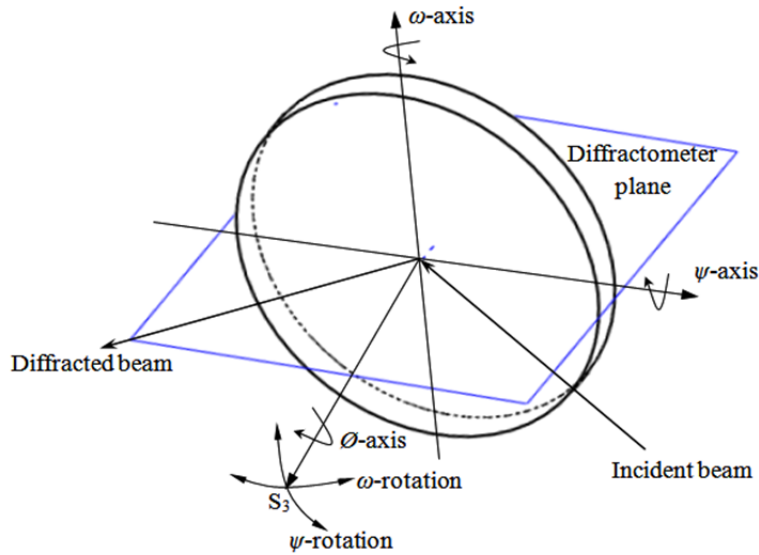


Fig. 3-5: Schematic view showing ψ tilt by iso-inclination (ω -rotation) or side-inclination (ψ -rotation).

The residual stress analysis was performed using a Panalytical X'Pert PRO MRD (Panalytical B.V., Almelo, Netherlands) high-resolution X-ray diffractometer equipped with a high temperature stage up to 1100°C in conjunction with a vacuum system using Cu-K α radiation, as shown in Fig. 3-6. An initial scan was performed with a diffraction angle of 2θ ranging from 10 to 150° to identify the diffraction peaks. A diffraction peak having a 2θ angle greater than 120° is usually recommended for the residual stress evaluation due to its greater sensitivity to the variation in the d -values according to the Bragg's law [64], where d is the interplanar spacing. Therefore, a diffraction peak at $2\theta = 125.2^\circ$ was selected for the residual stress determination based on the pre-scan diffraction pattern of the coated sample. The XRD spectra surrounding this peak were scanned with a tilt angle of ψ from -40° to +40° in 9 steps at each temperature. For the coatings tested at elevated temperatures, the sample stage was heated from room temperature to 750°C in steps of 250°C. At each temperature, a minimum of 15 minutes was waited to allow the sample to reach thermal equilibrium. To coordinate the highly sophisticated movements of the X-ray source, detector, and sample stage tilting, X'pert Data Collector software (Panalytical B.V.) was used to automate the measurement and data collection. The analysis of the measured data was performed using X'pert Stress software (Panalytical B.V.). The peak profile was evaluated using the constant + range background correction method and fitted with a parabolic function to identify the center position of the peak [65].



Fig. 3-6: Panalytical X'Pert PRO MRD X-ray diffractometer.

3.3 Microstructural analysis

The deposited samples were first mounted in epoxy to protect the coatings, sectioned using a slow diamond cutter, re-mounted in epoxy, ground with sand papers up to a grit of #1200, and then polished using diamond polishing suspensions. The polished samples on MG 0.2 substrates were examined with a scanning electron microscope (SEM) (JSM-6380LV, JEOL Co. Ltd., Akishima, Japan) as shown in Fig. 3-7. While, polished samples on LSM/YSZ + MG 2.0 were examined with Hitachi S-4500 field emission SEM (University of Toronto) operating in backscattered mode with an accelerating voltage of 20 kV. The thickness of the electrolyte layer

was calculated from coating weights and adjusted by multiplying by a thickness-to-weight gain ratio determined from image analysis of selected coatings.



Fig. 3-7: The JSM-6380LV SEM system with EDS.

3.4 Microhardness test

Vickers microhardness tests were performed on the polished cross-section using a computerized Buehler micro-hardness testing machine (Micromet-5100) as shown in Fig. 3-8. A load of 100 g and dwell time of 15 seconds were used during testing. The reported value represents an average of 10 measurements in each condition. Before the actual tests, a calibration of the machine was performed using standard reference calibration block. The indentation was made in the center of

the coating by carefully locating it under a microscope, and all the indentations were adequately spaced to avoid any potential effect of strain field caused by adjacent indentations.



Fig. 3-8: A Buehler Micromet-5100 Vickers microhardness tester.

3.5 Fracture toughness using Vickers indentation technique

Fracture toughness measurements were performed using Vickers indentation technique as discussed above. The coating made with a spray condition of G2 (Table 3-1) with MG 0.2 substrate, which had a torch power of 133 kW and a stand-off distance of 90 mm, was selected for the fracture toughness measurement. The sample was cut using a slow diamond cutter, mounted in epoxy, ground with sand papers up to a grit of #1200, and then polished using diamond paste on the top surface. Vickers microhardness tester as shown in Fig. 3-8 was used for the indentation on the polished top surface of the sample. A load of 200 g and dwell time of 15

seconds were used during testing. The indentation was made in the center of the coating by carefully locating it under a microscope, and all the indentations were adequately spaced to avoid any potential effect of strain field caused by adjacent indentations as well. The SEM observations were carried out to measure the crack length for each indentation. Also, the reported value represents an average of 10 measurements.

3.6 Interfacial indentation test

The interface fracture toughness of the coatings was evaluated from a Vickers interface indentation test. The schematic representation of this test is shown in Fig. 2-6. Analysis by indentation was performed on a cross-section of the coating deposited on MG 0.2 substrate with a torch power of 133 kW and a stand-off distance of 90 mm. The indentations were performed on a Vickers microhardness tester (Micromet-5100) using loads of 50g, 100g and 200g and dwell time of 15 seconds. Five indentations were performed at each level of load in order to determine a reliable mean crack length. The diagonal of the indent was carefully located to coincide with the coating-substrate interface. The indentations were examined by SEM.

Chapter 4: Results and Discussion

The focus of this chapter is to present the evolution of residual stresses in the YSZ electrolyte coatings deposited by the suspension plasma spraying. Initially, XRD characterization of deposited YSZ coating was studied. The work done on the room-temperature behavior of YSZ coating is presented first, followed by the work done on the high-temperature behavior of YSZ coating. This separation is motivated by substantial changes in the residual stress observed at higher temperatures compared to room temperature. The high temperature residual stress at a typical SOFC operating temperature is studied, and potential stress relaxation mechanisms were discussed. At room temperature, residual stress, microstructure and hardness are all characterized and considered within the context of the observed variation with deposition process conditions and with a different substrate. Lastly, the characterization of fracture toughness and interface fracture toughness was performed for the sample made in the optimized process condition.

4.1 XRD characterization

The most significant factor contributing to conductivity in SOFC is the phase constitution of the electrolyte. Figure 4-1 shows the XRD pattern of YSZ powder and SPS YSZ coating. The diffraction analysis showed that all peaks are associated with cubic YSZ in both YSZ powder and sprayed YSZ coating, and there was no variation in the diffraction peak position. This indicates that phase and chemical composition remained unchanged during the SPS process. The cubic phase in Zirconia provided the highest conductivity [66]. Furthermore, it was observed that the diffraction peak of as-sprayed coating had a higher intensity than that of powders, which

indicates that the SPS plays a role in grain refinement, and therefore, can produce a fine and dense coating. This result is in agreement with the literature [67]. This is an important characteristic of SOFC electrolyte to reduce leakage and achieve high power density. A smaller grain size is also likely to improve the flatness of the sheets for use in SOFC stacks as investigated by Bellon *et al.* [68]. Also, this grain refinement improves the mechanical properties as well according to the well-known Hall-Petch relationship, and thereby, the performance of the coatings.

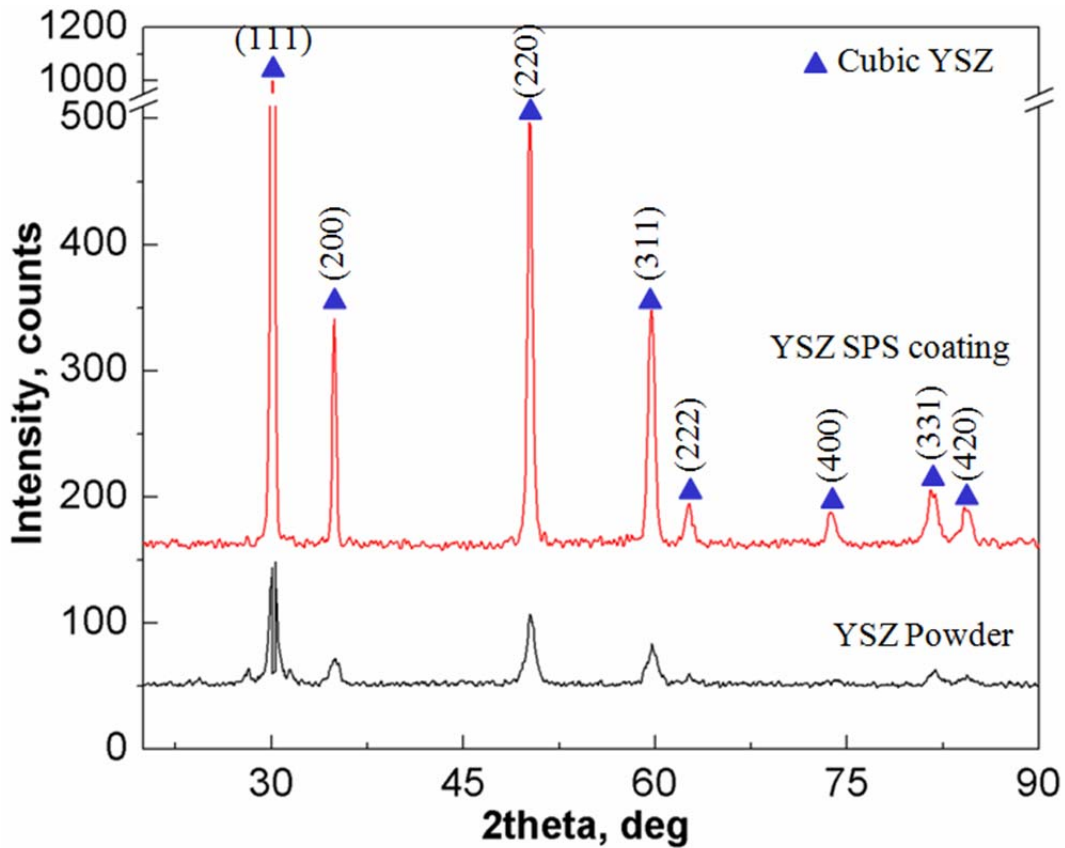


Fig. 4-1: XRD patterns of YSZ powder and SPS YSZ coating.

4.2 Residual stresses

Residual stresses in the SPS coatings can originate from the large thermal gradient experienced during the deposition process. As discussed earlier, residual stresses can be sub-divided into two main contributions: quenching stress or primary stress, and thermal mismatch stress or secondary stress. The quenching stress rises as individual splats rapidly solidify and cool from a molten state to the substrate temperature, while their contraction is restricted by adhesion to the substrate. These quenching stresses are always tensile. Thermal mismatch stress develops during post-deposition cooling to room temperature due to the difference in the CTEs between coating layers and substrate [51]. Thermal mismatch stress can be either tensile or compressive, depending on the relative values of the CTEs of the coating layers and substrate. In the present case, the thermal mismatch stress in the YSZ layer is compressive, because the CTE of 8YSZ (10.5 ppmK^{-1}) is lower than that of both the LSM-YSZ cathode (11.7 ppmK^{-1}) and the 430 stainless steel substrate (11.4 ppmK^{-1}) [69-71].

4.2.1 Surface roughness

It should be noted that coating roughness (R_T) has to be considered in comparison with the mean X-ray penetration depth ($\tau_{0.3}$) at a tilt angle corresponding to $\sin^2\psi=0.3$ while performing the XRD measurement. If $R_T \ll \tau_{0.3}$, the roughness would not play a significant role [65]. If $R_T \geq \tau_{0.3}$, the stress relaxation in the asperities can contribute to a lower value of the measured residual stress. On the other hand, surface modification techniques that decrease the roughness, e.g.,

grinding and polishing, can alter the stress state to a significant extent. The mean X-ray penetration can be calculated using the following equation [54],

$$\tau_{0.3} = -\frac{\sin \theta \cos \psi \ln(1 - G_\tau)}{2\mu}, \quad (4.1)$$

where τ is the penetration depth, μ is the linear absorption coefficient, and G_τ is the fraction of the total diffraction intensities contributed by the surface layer of thickness τ . A G_τ value of 0.99 was calculated using Bragg-Brentano geometry for the electrolyte thickness of 45 μm . In the present study, the calculated mean X-ray penetration depth was 27 μm , based on a wavelength of $\lambda=1.5406 \text{ \AA}$ and a bulk density of 5.96 g/cm^3 of YSZ [72], which is higher than the measured roughness of approximately 8 μm . Therefore, the effect of coating roughness on the residual stress was not considered.

4.2.2 X-ray diffraction and $\sin^2\psi$ measurements

Figure 4-2 shows a typical XRD pattern from an initial scan over the electrolyte top surface. The (531) diffraction peak positioned at a 2θ angle of 125.2° indicated by an arrow in the figure is selected for the subsequent residual stress measurements. All the peaks in the diffraction pattern correspond to those of the cubic YSZ, and there are no peaks from the LSM in the intermediate cathode layer or of the porous 430 stainless steel substrate. This indicates that X-ray did not penetrate into the intermediate cathode layer and the bottom porous 430 stainless steel support. The phase diagram of 8 mol% YSZ indicates that this cubic structure remains stable at SOFC operating temperatures of 650-800°C [73].

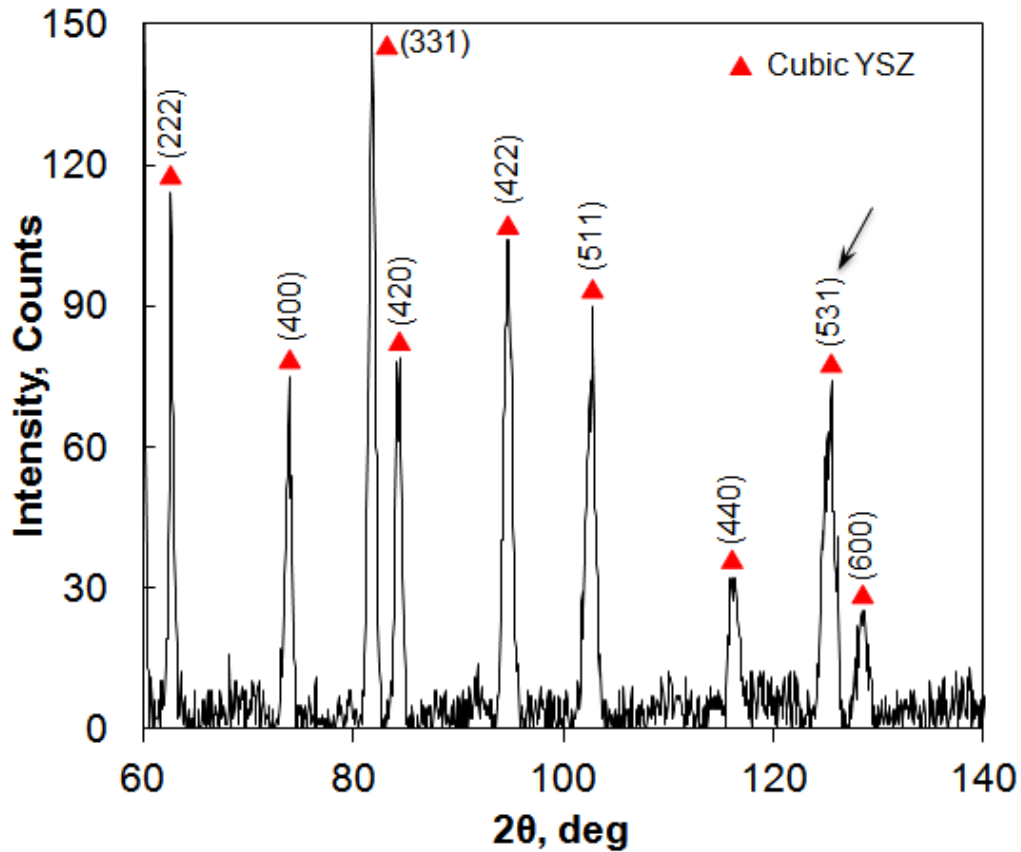


Fig. 4-2: XRD pattern for the YSZ electrolyte of a metal-supported SOFC half-cell.

Figure 4-3 shows the change of the diffraction peak from the selected (531) plane with the tilt of ψ . It is seen that the (531) peak position shifts to lower angles with increasing ψ , indicating that the inter-planar spacing (d) increases. This behavior suggests that the residual stress in the surface layer is tensile in nature, which means that the quenching stress is larger than the thermal mismatch stress. This result is likely due to the fairly small differences between the CTEs of the three component layers. The peak profiles were fitted with parabola in order to determine center of the peak profile.

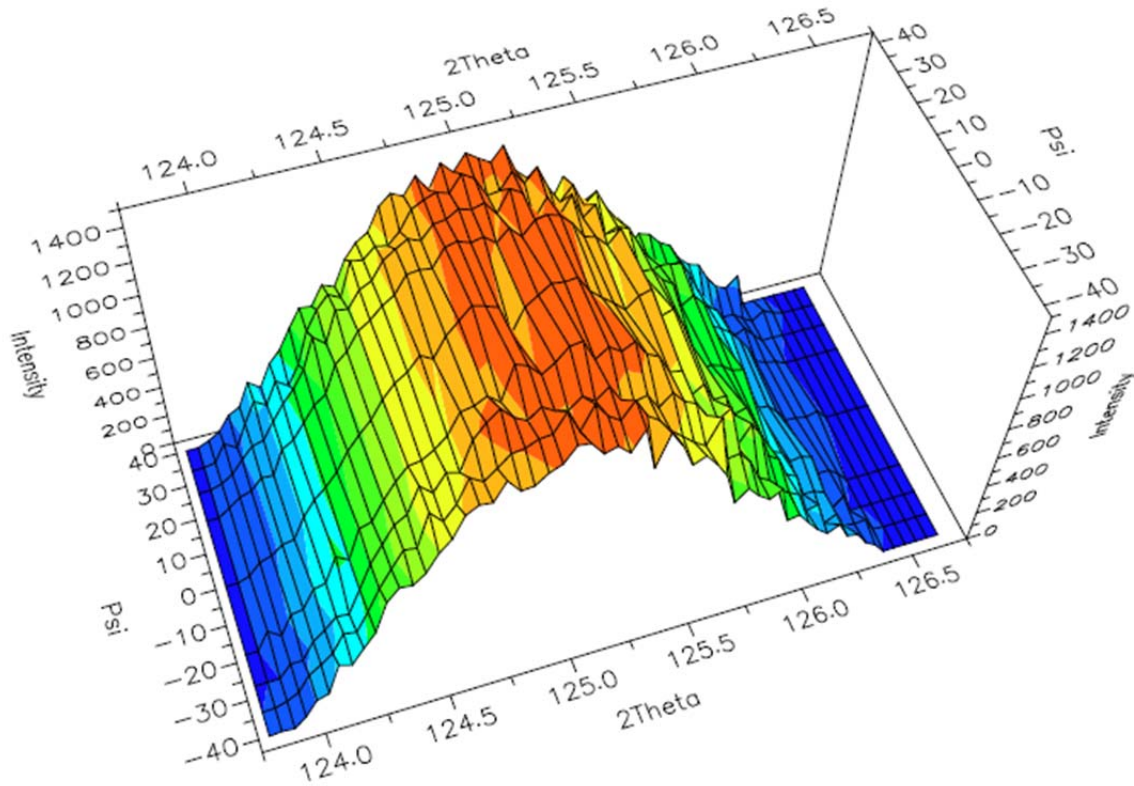


Fig. 4-3: XRD patterns showing the change of the (531) plane diffraction peak of the YSZ electrolyte with ψ at room temperature.

Figure 4-4 shows a typical ϵ - $\sin^2\psi$ diagram for the (531) diffraction plane in the YSZ electrolyte, where diamonds indicate negative ψ tilt, triangles indicate positive and zero ψ tilt, and the solid line represents the linear least-square fitting to both sets of data points. Although the data are somewhat scattered, the lattice strain ϵ increases approximately linearly with increasing $\sin^2\psi$. Residual stress can thus be estimated from the slope of the ϵ - $\sin^2\psi$ best fitting line based on Eq. 2.5, mentioned earlier. It should be noted that the elastic constant of the coating would be different from bulk values due to the presence of porosity, micro-cracks, and other process-related microstructural features. Furthermore, the strain is measured specifically in the direction perpendicular to the (531) plane. Therefore, the corresponding elastic constant (Young's

modulus) E and Poisson's ratio ν are required to convert the measured strain into stress [74]. Santtonay *et al.* [75] had calculated X-ray elastic constant for the (531) plane from compliances with the Hill-Neerfeld model and derived $E_{(531)}$ and $\nu_{(531)}$ of 8 mol% YSZ. These values were used in the present analysis as a baseline value. Since the elastic constants for the (531) plane at elevated temperatures are not available, it is assumed that the temperature-dependent elastic constant for the (531) plane of 8 mol% YSZ follows the same trend as that of the bulk modulus as a function of temperature as determined by Huang and Harter [28] via a linear least square fitting. The temperature-dependent $E_{(531)}$ values given in Table 4-1 were estimated on the basis of a room-temperature elastic constant for the (531) plane given in [75] (i.e., $E_{(531)} = 242$ GPa).

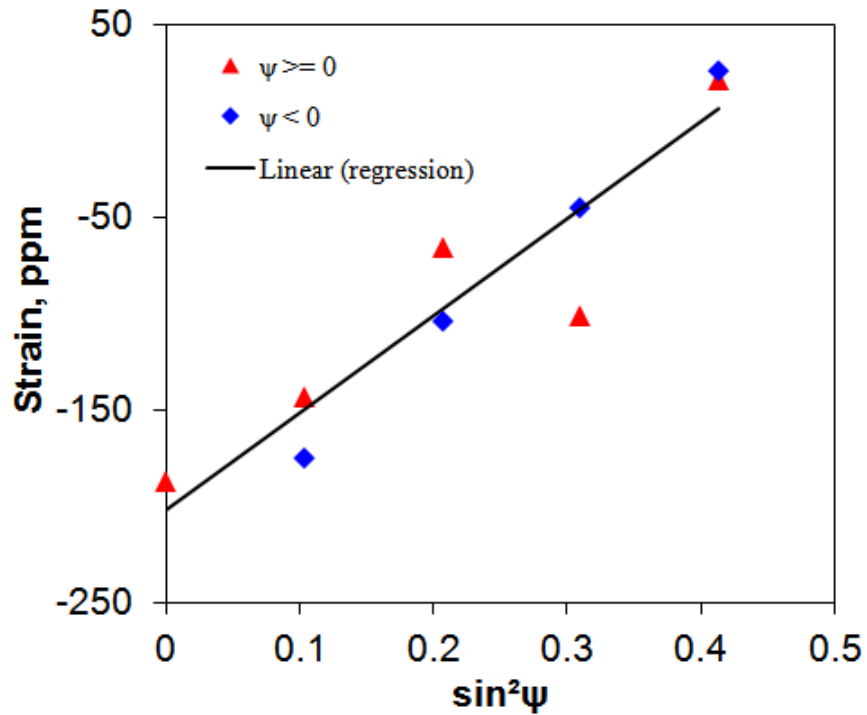


Fig. 4-4: ϵ - $\sin^2\psi$ diagram for the (531) diffraction plane of the YSZ electrolyte determined at room temperature, where the solid line represents the linear least square fitting.

4.2.3 Temperature dependent residual stress

Figure 4-5 shows the residual stress as a function of temperature in the YSZ electrolyte made with the G2 processing condition with a torch power of 133 kW and a stand-off distance of 90 mm (Table 3-1). At room temperature, the residual stress is tensile, with a value of approximately 90 MPa. The tensile residual stress decreases with increasing temperature. At a typical SOFC operating temperature of 750°C, the residual stress of the electrolyte becomes approximately 39 MPa. As mentioned above, the presence of tensile residual stress suggests that the quenching stress is greater than the thermal mismatch stress.

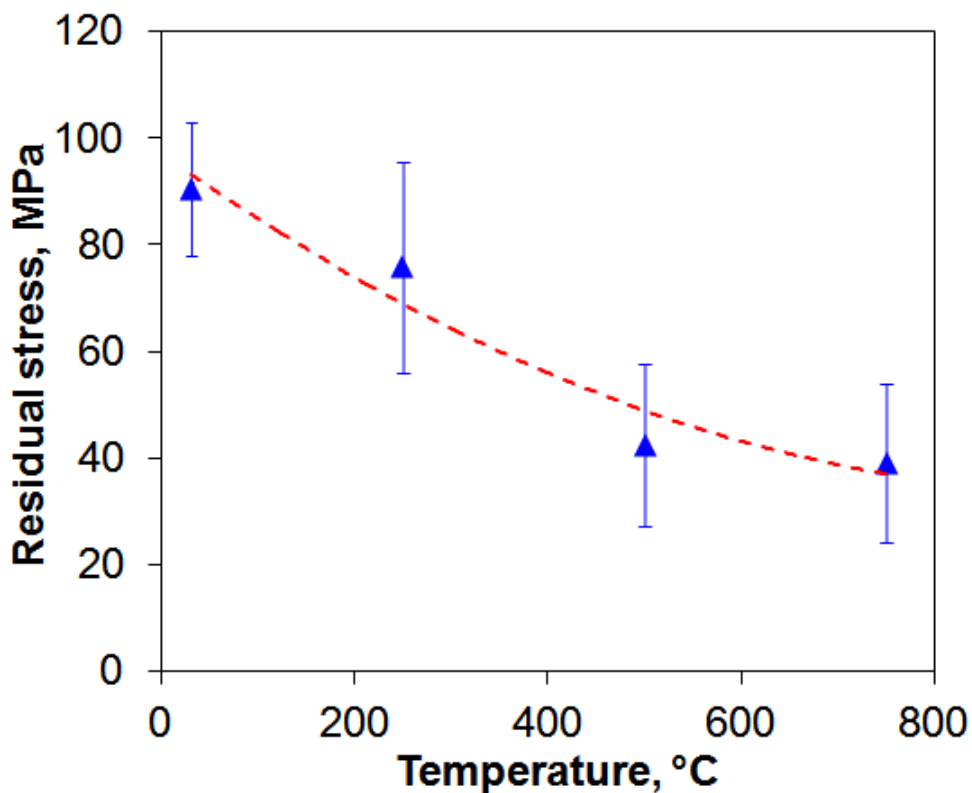


Fig. 4-5: Residual stress in the YSZ electrolyte fabricated using process condition G2 (a torch power of 133 kW and a stand-off distance of 90 mm) as a function of temperature.

The magnitude of residual stress depends in part on the nature of the microstructural attributes of a coating. Figures 4-6 and 4-7 show typical SEM images of the electrolytes fabricated with the G2 processing condition before the high-temperature XRD measurement was performed. It is seen that three main types of defects are present in the YSZ electrolyte layer: microcracks, micro/macro porosity, and segmentation cracks (vertical cracks), as shown in Fig. 4-6 and 4-7. The microcracks and porosity are considered as an intrinsic part of the coating and can be reduced by modifying spray processing parameters. Microcracks are generated primarily during quenching of the molten splats to relieve the tensile stresses. The micro/macro porosity occurs by a number of mechanisms, including incomplete penetration of molten splats into surface crevices and the inclusion of partially melted particles in the coating [24,76]. The segmentation cracks run through most the coating thickness, and some cracks even penetrate into the underlying cathode layer as shown in Fig. 4-7. They also form to relieve the tensile stresses during solidification of the coatings. Several previous studies have also shown the presence of segmentation cracks in the suspension plasma sprayed coatings [25,77-79]. It should be noted that while the microcracks and porosity provide localized stress relaxation, the segmentation cracks provide a stress relief for larger sections of the coating. While all of these defects could potentially increase gas leakage through the electrolyte layer, the segmentation cracks could be unfavourable to the power density and efficiency of the cell by providing a certain gas leakage pathway.

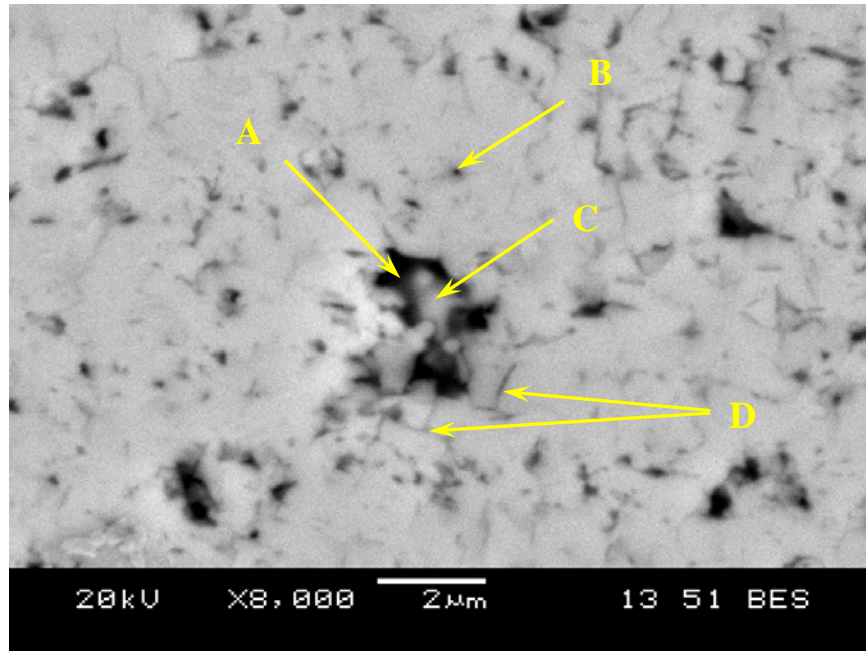


Fig. 4-6: A higher magnification SEM cross-section image of SPS YSZ coating showing A- macro porosity, B-micro porosity, C- un/partially melted particle, D- microcracks.

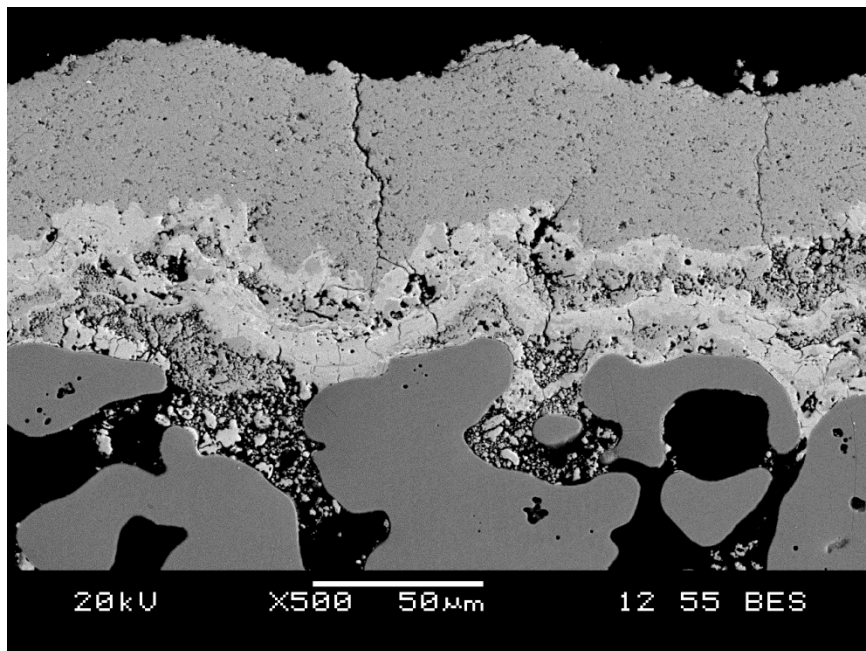


Fig. 4-7: SEM cross-section image of SPS YSZ coating showing segmentation cracks.

Several mechanisms may be associated with the change of residual stresses at high temperatures shown in Fig. 4-5. These factors include changes in the Young's modulus of the YSZ electrolyte, thermal expansion mismatch between component layers, generation of new micro-defects and creeping of porous stainless steel substrate. First, the Young's modulus of YSZ decreases with increasing temperature, as shown in Table 4-1. This decrease would result in a decrease in the residual stress with increasing temperature. A similar change in the Young's modulus of YSZ has been reported [80,81]. Second, increasing the temperature from room temperature to 750°C would change the thermal expansion mismatch between the YSZ electrolyte, LSM/YSZ cathode, and stainless steel substrate. Church *et al.* [82] showed that both the CTEs of 430 stainless steels and of 8 mol% YSZ increase with increasing temperature, but that the CTE of 430 stainless steels exhibits a steeper increase than that of 8 mol% YSZ. This implies that somewhat more thermal mismatch would be generated, which would slightly increase the tensile stress in the electrolyte layer. It is speculated the increase in temperature may have resulted in the generation of new micro-defects, which additionally relieved residual stress in the electrolyte layer. However, it is difficult to quantify this factor solely by SEM cross-section image as shown in Fig. 4-8. Berndt [83] previously detected the phenomenon of microcracking in a 12 wt% YSZ coating undergoing thermal cycling by an acoustic method.

Another potential mechanism at higher temperatures is the presence of creep of the porous stainless steel substrate. Creep deformation becomes relevant to a material at temperatures near half of its melting point [12]. The melting point of 430 stainless steels is reported to begin at 1427 °C [84]. Then the creep would be expected to occur when the test temperature is above ~710 °C. Indeed, as pointed out by Liu *et al.* [12] the potential creep deformation of the SOFC

support structure should not be neglected at typical cell operating temperatures of 650-800°C. The creep behavior of porous 430 SS is not available in the open literature. However, it is speculated that the presence of creeping in porous stainless steel support would help to reduce the residual stress in the electrolyte layer at 750 °C. This proposed stress relaxation mechanism is highly speculative, and more studies would be required to evaluate its potential contribution. Therefore, the decrease of the residual stress with increasing temperature (Fig. 4-5) is a consequence of the combined changes in the Young's modulus, thermal expansion mismatch, generation of new micro-defects as well as the possible creep deformation in the porous stainless steel substrate.

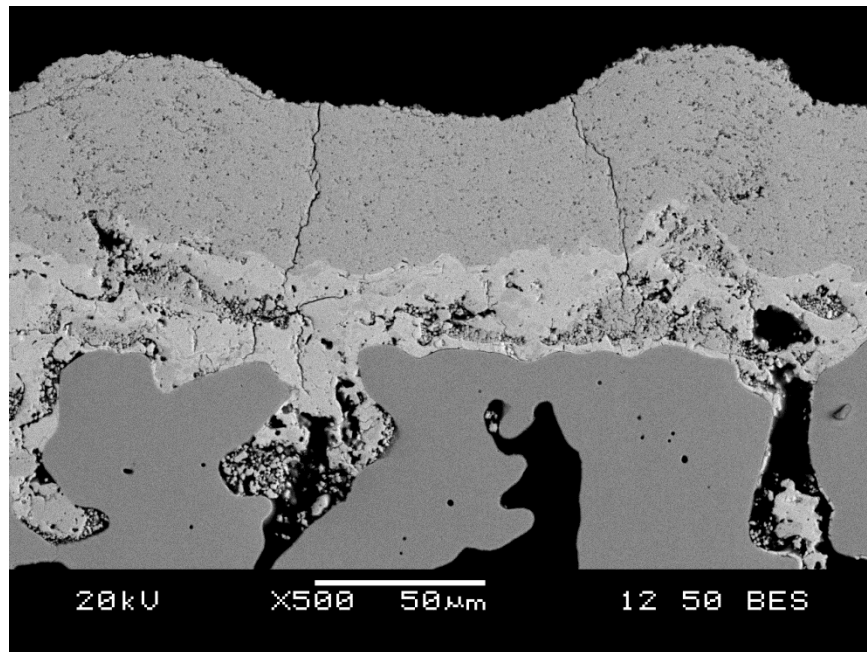


Fig. 4-8: SEM cross-section image of SPS YSZ coating after high temperature test.

Table 4-1: Residual stresses at different temperatures in the YSZ electrolyte fabricated with G2 spray condition (a torch power of 133 kW and a stand-off distance of 90 mm) along with the corresponding values of $E_{(531)}$ and $\nu_{(531)}$.

Temperature, °C	$\nu_{(531)}$	$E_{(531)}$, GPa	σ, MPa
RT	0.35 [75]	242 [75]	91 ± 13
250	0.35	218	76 ± 20
500	0.35	195	43 ± 15
750	0.35	173	39 ± 15

From the above results, it is clear that the residual stresses in the YSZ electrolytes of porous 430 stainless steel-supported SOFC half-cells are tensile in nature, and they decrease with increasing temperature. The occurrence of some vertical cracks in the YSZ electrolyte (Fig. 4-7) corroborates this point, since the compressive residual stress would not cause such segmentation cracks. Indeed, the measured residual stress (Fig. 4-5) via the XRD is a “remaining” stress in the YSZ electrolyte because the formation of cracks during fabrication relieves some of the residual stresses. This would be the reason why the determined tensile residual stresses in the electrolytes are lower than the tensile fracture strength of ~200 MPa or bending fracture strength of ~350 MPa of free standing 8YSZ [85]. The present study on the residual stress would provide an input for understanding the mechanical properties such as flexural strength, fracture toughness and adhesion strength and for better estimating the performance, structural integrity and durability of SPS YSZ electrolyte in the metal-supported SOFCs.

4.3 Influence of torch power and stand-off distance

Residual stresses in the plasma sprayed coatings are known to vary significantly with deposition conditions. Torch power and stand-off distance are two key factors in controlling the performance and stress state of coatings. Therefore, microstructure, residual stress and microhardness versus varying torch powers and stand-off distances listed in Table 3-1 were evaluated. Furthermore, two different substrates of LSM/YSZ + MG 2 and MG 0.2 were used to analyze the effects of substrates on residual stresses and microstructure. The impacts of the plasma spray process parameters and substrates on the coating characteristics and properties have been studied by means of classical one-factor-at-a-time approaches. As shown in Table 3-1, the plasma torch input power for spray conditions G4, G2 & G5 were 100 kW, 133 kW and 162 kW, respectively, with a constant stand-off distance of 90 mm and the stand-off distance for spray conditions G1, G2 & G3 were 70 mm, 90 mm and 120 mm, respectively, with a constant torch power of 133 kW.

4.3.1 Effects on microstructure

All YSZ coatings show a typical microstructure containing solidified splats, porosity, microcracks and segmentation cracks as discussed earlier. Cross-sectional SEM micrographs of SPS YSZ coatings on LSM/YSZ + MG 2 substrate, under different torch powers and stand-off distances are presented in Fig. 4-9. It is clear that the porosity of YSZ coatings decreases as the torch power increases. Similar behavior has been observed by other [86]. With a lower torch power, plasma enthalpy may not have been adequate to fully evaporate suspension liquid and

completely melt powder particles [87]. This would result in un- or partially-melted particles in the coating. When they impacted on the substrate or on the already formed splats, they were not able to spread out completely to form splats and therefore, could not conform to the surface. In such cases the inter-lamellar pores would be formed due to the solidification of the splats. Moreover, when the applied power was relatively low, during the cooling process the microcracks and pores could be formed at the boundary of the un-melted particles and around splats, as shown in Fig. 4-6. Among the conditions tested, coating with lower torch power of 100 kW showed the highest porosity in the coating. With increasing torch power, denser coatings with an improved inter-splat adhesion were formed [86-88]. On the other hand, there was also a greater heat flux from the plasma to the coating and the substrate, which promoted the formation of cracks in the coatings due to the high-heat input and the resulting higher temperature gradient. Segmentation cracks were observed in all the coatings with LSM/YSZ + MG 2 substrate, as also reported in [25,77-79]. More segmentation cracks could be seen with increasing torch power. Linear crack densities have been previously used to assess the severity of segmentation cracking (e.g. [89]). However, this parameter was noted to be not a good indicator of crack severity in the electrolytes in this study because the cracks in the various coatings had widely differing characteristics.

The spray distance is another important parameter which affects the microstructure of YSZ coatings. It was observed earlier that particle flattening behavior depended on the velocity and temperature of particles and therefore, depended on the stand-off distance [90]. Particles are melted in the high-temperature plasma flame and accelerated towards the substrate where it rapidly solidifies. The spray distance determines the velocity of melted particles when they

impact the substrate. At a smaller stand-off distance of 70 mm, particles have higher velocity and greater heat flux to the substrate compared with the coatings produced at a larger stand-off distances of 120 mm. This creates a steep temperature gradient in the coating with high surface temperatures. This is indeed similar to the situation with a high torch power as discussed above. In contrast, at a larger stand-off distance of 120 mm the heat input and temperature gradient would become lower, results in a higher porosity, equivalent to the situation with a low torch power as mentioned above. Bacciochini *et al.* [91] also reported that the larger stand-off distances lead to coatings with more porosity and reduce inter-splat adhesion. This can be explained as at a larger spray distance, plasma likely cooled to the point that, significantly more molten particles began to re-solidify before striking the substrate [92]. This results in a higher portion of partially/un-melted particles in the coating and therefore, increases porosity in the coating. Based on the above discussion, it could be concluded that the coating fabricated with a torch power of 133 kW and a stand-off distance of 90 mm (G2), is better because of its denser microstructure as well as better integrity. Furthermore, in this coating micro-pores are uniformly distributed, and macro-pores are few as shown in Fig 4-9(b), which implies its higher bonding strength. Therefore, this condition could better meet the dense and gas-tight requirements of electrolyte for SOFCs.

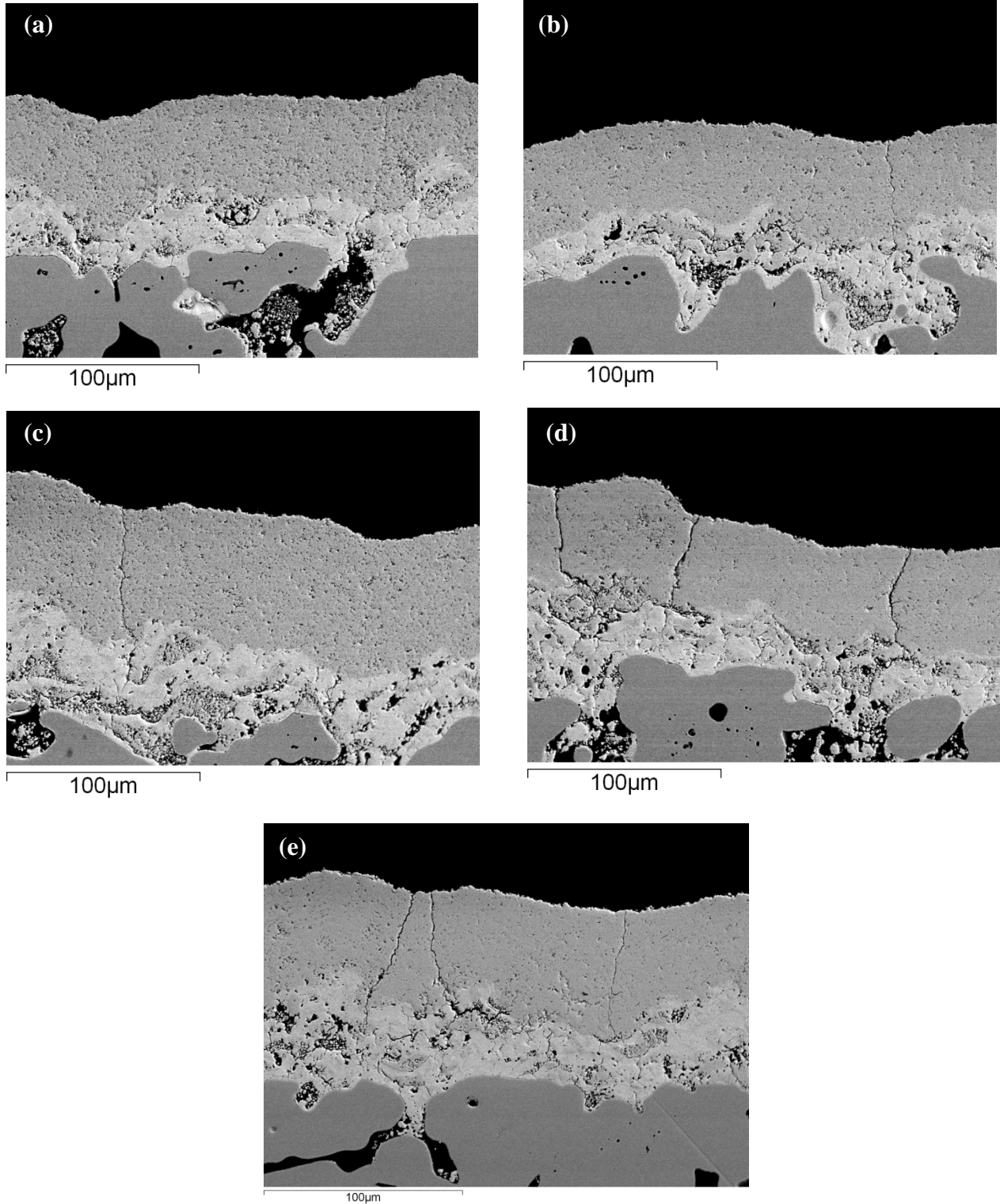


Fig. 4-9: SEM cross-section images of YSZ on LSM/YSZ + MG 2 substrate, (a) 100 kW, 90 mm, (b) 133 kW, 90 mm, (c) 133 kW, 120 mm, (d) 133 kW, 70 mm, and (e) 162 kW, 90 mm.

Figure 4-10 shows typical SEM micrographs of YSZ coatings on MG 0.2 substrates. Unlike LSM/YSZ + MG 2 substrate (Fig. 4-9), no segmentation cracks were observed in this coating except G1 (70 mm), G2 (133 kW) and G5 (162 kW). Furthermore, it can be seen that the segmentation cracking is less severe and does not penetrate throughout the coating thickness as in the case of LSM/YSZ + MG 2 substrate. For example, in Fig. 4-9(d) some cracks penetrate into the cathode (LSM/YSZ) layer. However, in Fig. 4-10(d) cracks are comparatively fine and stop within the coating. Also, coatings on MG 0.2 substrate are smooth than coatings on LSM/YSZ + MG 2 substrate as shown in Fig. 4-9 and Fig. 4-10.

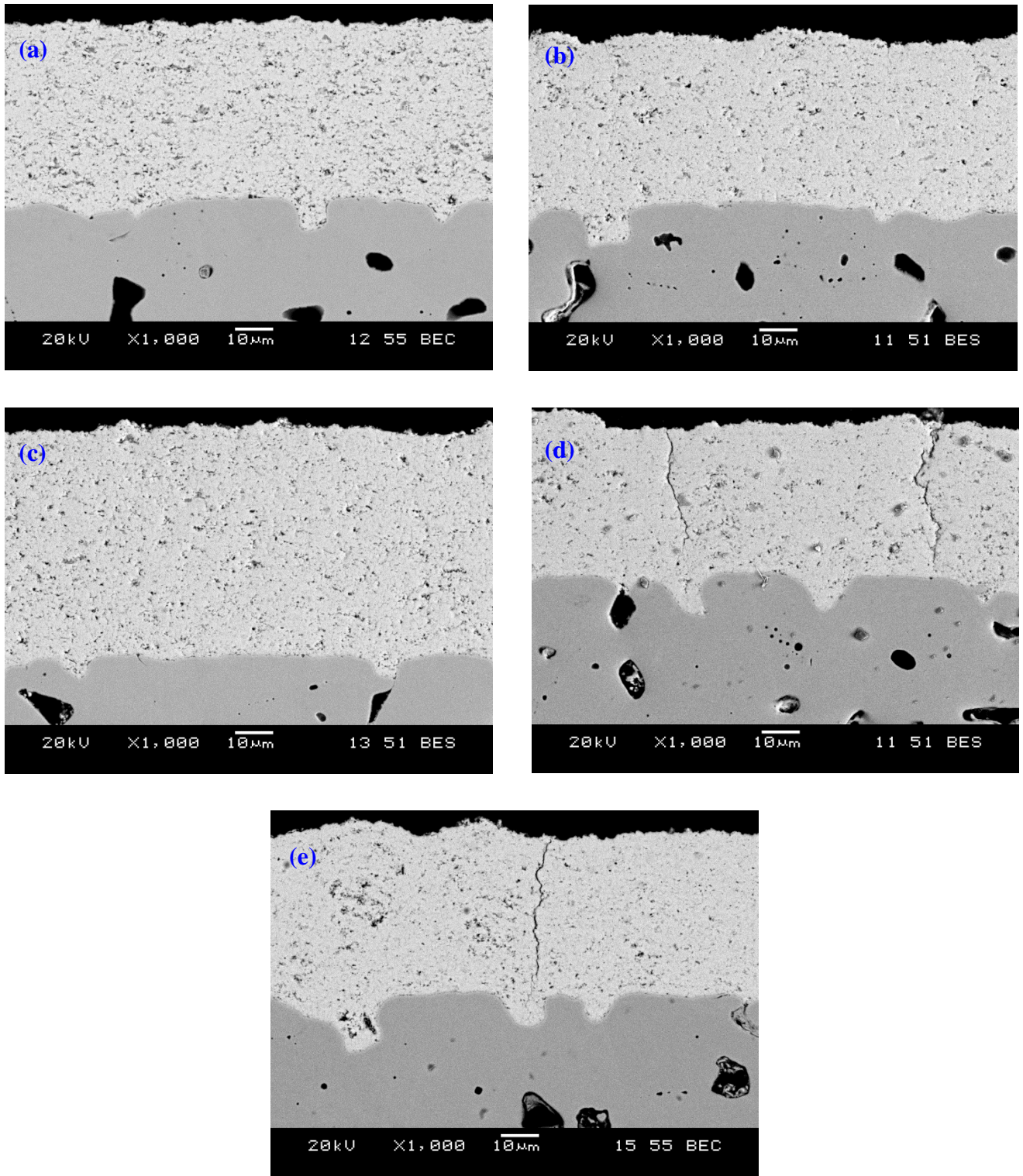


Fig. 4-10: SEM cross-section images of YSZ on MG 0.2 substrates, (a) 100 kW, 90 mm, (b) 133kW, 90 mm, (c) 133 kW, 120 mm, (d) 133 kW, 70 mm, and (e) 162 kW, 90 mm.

4.3.2 *Effects on residual stress*

Figure 4-11 and Figure 4-12 show the variation of residual stresses with torch power and stand-off distance, respectively, using processing conditions given in Table 3-1. It was observed that the residual stress was tensile in all the conditions. As discussed earlier, the residual stress profile was made up mainly from the quenching stress, and the thermal mismatch stress was relatively small. This was due to smaller differences in the CTE of the selected coating/substrate combination. A similar trend was observed on both substrates with varying torch powers and stand-off distances. The residual stress initially increases with increasing torch power and stand-off distance, reaches to the maximum value and then starts decreasing with the further increase in the torch-power and stand-off distance. These changes in the residual stress were attributed to the change in the microstructure with varying torch powers and stand-off distances. At the lower torch power (100 kW), it was observed that the residual stress in YSZ coating was lower compared to 133 kW torch power. This was mainly attributed to its relatively higher porosity, which resulted in a stress relaxation through pores. With increasing torch power, the residual stress increased due to the decrement in the porosity. With further increasing torch power the formation of segmentation cracks relieved the tensile residual stresses. As a result, the highest residual stress observed at a torch power of 133 kW was related to a combined effect of the increase in the coating density and the increase in the segmentation cracks in coating on LSM/YSZ + MG 2 substrate or the formation of segmentation cracks in coating on MG 0.2 substrate. At the highest torch power of 162 kW, the increase in the cracks was more prominent than the increase in the coating density due to the higher temperature gradient generated during the plasma spraying process. Consequently, this condition showed a lower magnitude of residual stress. Similar to the higher torch power of 162 kW, a smaller stand-off distance of 70 mm also

showed more prominent cracks in the coating due to the relief of more tensile residual stress. Likewise, in the case of a larger stand-off distance, a higher amount of porosity resulted in a lower residual stress in the coating. The coating deposited on MG 0.2 substrate showed a higher residual stress at a lower torch power of 100 kW or a larger stand-off distance of 120 mm, and a higher torch power of 162 kW or a smaller stand-off distance of 70 mm compared to the coatings deposited on LSM/YSZ + MG 2 substrate. Unlike LSM/YSZ + MG 2, the coating deposited on MG 0.2 substrate at a lower torch power of 100 kW and a longer stand-off distance of 120 mm did not show the formation of segmentation cracks and therefore, resulted in a higher value of residual stresses. Furthermore, at a higher torch power and shorter stand-off distance on MG 0.2, the segmentation cracks did not penetrate all the coating thickness and therefore, they appeared to be less severe than LSM/YSZ + MG 2. It follows that the residual stresses were higher in these conditions on MG 0.2 substrate. The fact that the measured residual stress reached the maximum in the coating produced with a torch power of 133 kW and a stand-off distance of 90 mm in condition G2, compared to all other conditions tested, might be due to its relatively dense microstructure without excessive cracks. The higher tensile residual stress in condition G2 would lower the coating resistance to inhibit crack propagation and therefore, result in a lower fracture toughness of YSZ electrolyte layer [56]. This may potentially lower the service life of the electrolyte layers. On the other hand, its relatively dense microstructure without excessive cracks would be an important attribute for its application as a SOFC electrolyte to achieve low leak rates and high power density. From the above analysis and the observed results, it could be concluded that the dependence of residual stresses on the torch power and stand-off distance was similar, but in a reverse order (i.e., a higher torch power corresponded to a smaller stand-off distance, or vice versa).

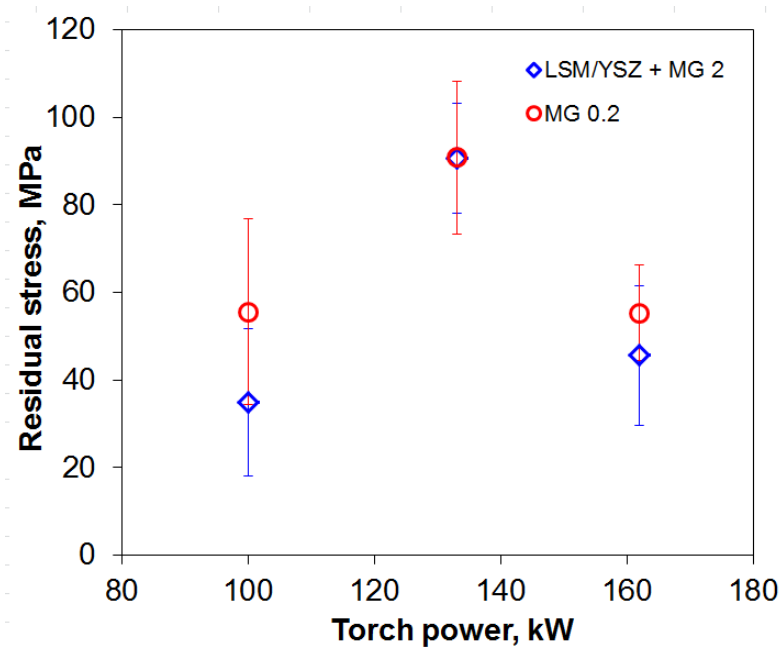


Fig. 4-11: Residual stresses in the YSZ electrolyte layer at room temperature as a function of torch power at a constant stand-off distance of 90 mm.

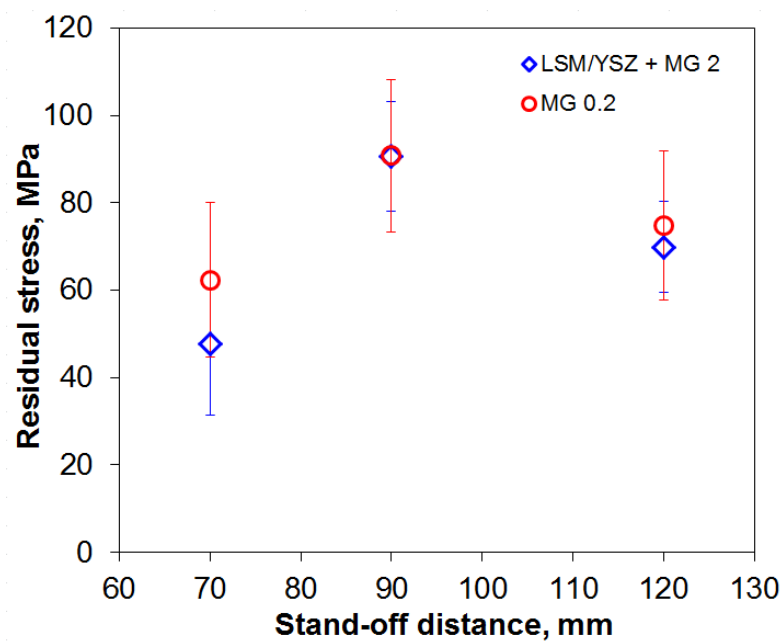


Fig. 4-12: Residual stresses in the YSZ electrolyte layer at room temperature as a function of stand-off distance with a constant torch power of 133 kW.

4.3.3 Effects on microhardness

The effect of torch power and stand-off distance on the coating microhardness is shown in Fig. 4-13 and Fig. 4-14, respectively. The microhardness was measured on the polished cross-section using a computerized Vickers microhardness tester at 100g load. The indentation was made at the center of the coating thickness to eliminate the effect of the free surface and underlying substrate. The distance between two indentations was not less than three times the diagonal to prevent stress field effects from nearby indentations. It was observed that with increasing torch power or decreasing stand-off distance, the micro-hardness of the coatings increased. This was due to the decrement of the micro-defects in the coatings. The measured values were in agreement with the reported values in the literature [93]. The micro-hardness of the coatings was influenced by the microstructure of the coating. Among several microstructural features, porosity seemed to have a stronger influence on the micro-hardness of the coating. It can be seen from Fig. 4-10 that with increasing torch power or decreasing stand-off distance, porosity in the coating reduced, which led to an increase in the micro-hardness. Chaim *et al.* [94] reported that the micro-hardness of 3wt% YSZ increased with decreasing apparent porosity or increasing bulk density. The high hardness observed at a torch power of 162 kW and a stand-off distance of 90 mm, was due to its lowest porosity. The lowest hardness in all test conditions was observed in the sample made with a torch power of 100 kW and a stand-off distance of 90 mm due to the presence of highest porosity.

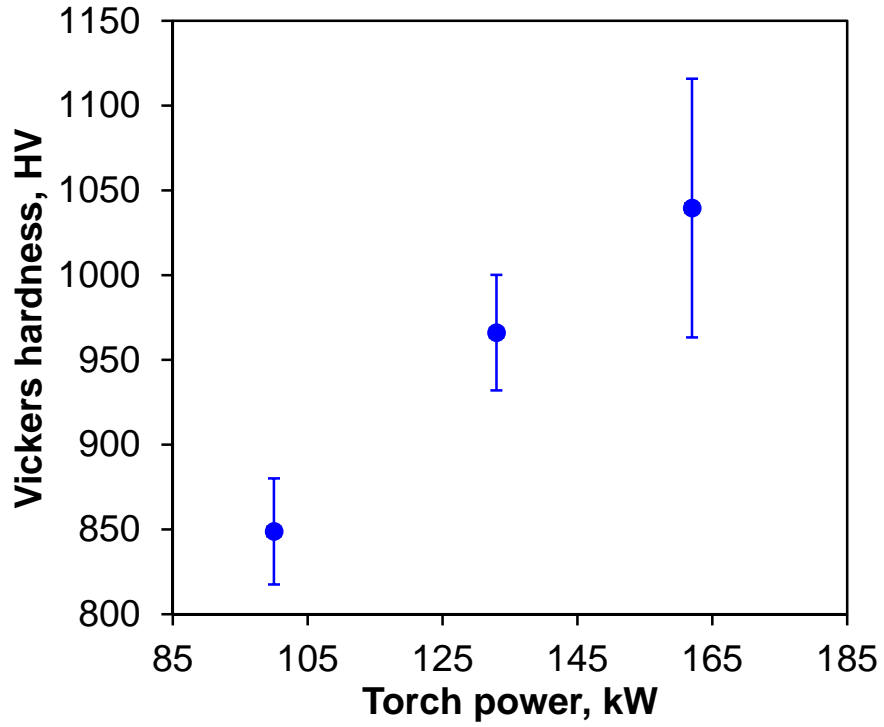


Fig. 4-13: Hardness as a function of torch power at a constant stand-off distance of 90 mm.

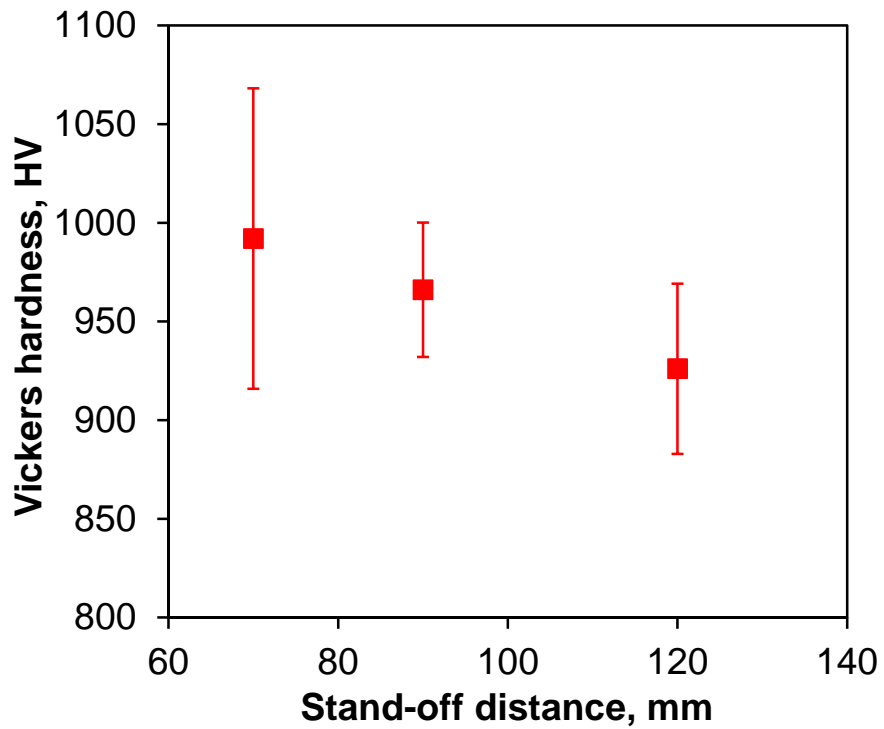


Fig. 4-14: Hardness as a function of stand-off distances at a constant torch power of 133 kW.

4.4 Fracture toughness

It should be noted that because of the simplicity of specimen preparation and the acceptance of a small specimen, the fracture toughness measured via Vickers indentations has been widely accepted [95-97]. The relationship between the fracture toughness and indentation crack length has been shown in Eq. 2.6 and Eq. 2.7. To meet the geometrical requirement of Eq. 2.6 and Eq. 2.7, the indentation depth should be less than 10% of the coating thickness. The indentation depth calculated for 200g load was 4 μm , which was smaller than 10% of the coating thickness of about 45-50 μm . Therefore, the present study satisfied the geometrical requirement of using Eq. 2.6 and Eq. 2.7. Figure 4-15 shows a typical SEM micrograph illustrating indentation crack propagation during Vickers indentation tests. The average value of fracture toughness calculated using Eq. 2.6 was $1.61 \text{ MPa m}^{1/2}$, which was in agreement with the value of $1.65 \text{ MPa m}^{1/2}$ that was reported for tap cast 8mol% YSZ [98]. As discussed earlier, the YSZ coating contained tensile residual stresses and therefore, the fracture toughness should be calculated in consideration of the presence of residual stresses as indicated in Eq. 2.7. As determined above, the coating with G2 process had a tensile residual stress of approximately 90 MPa. Then the fracture toughness considering the presence of the tensile residual stress became $2.04 \text{ MPa m}^{1/2}$.

The fracture toughness of the coating depended on the microstructure of the coating. Porosity strongly affected the fracture toughness of the YSZ coating. The low porosity and improved inter-splat adhesion in condition G2 would enhance the ability to impede crack formation and propagation by an indenter. In this view, a lower porosity and higher inter-splat adhesion improved the fracture toughness of the coating. It could be deduced that the inter-splat cohesion

was the most important factor, which would significantly influence the fracture toughness. As the fracture along the splat interface could be used for the evaluation of the cohesive property among the splats, to a certain extent, it could thus be postulated that the fracture toughness was arguably capable of demonstrating cohesion among the splats.

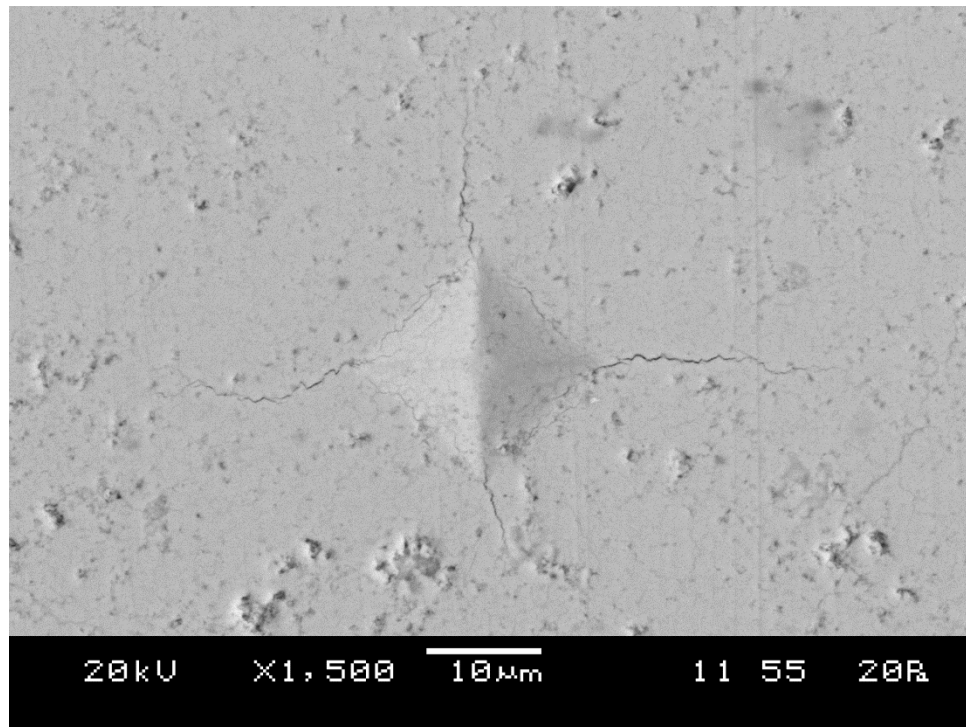


Fig. 4-15: A typical SEM micrograph showing indentation crack propagation.

4.4.1 Interfacial fracture toughness

A number of methods have been proposed to evaluate the adhesion between a coating and its substrate through normal or cross-sectional interfacial indentation tests. The indenter is used as a means to create interfacial cracks, which are then measured as a function of the applied load and treated in the context of fracture mechanics to obtain either interfacial fracture toughness or a

critical energy release rate, both of which are considered representative of the adhesion. The method used in the present work was developed by Lesage and Chicot [64] with reference to the determination of fracture toughness of brittle materials by indentation tests. Liu *et al.* [99] and Lesage *et al.* [100] have pointed out the influence of many parameters upon the value of the critical load such as the coating thickness, the state of residual stresses in the coating, and the nature of both materials. A numerical simulation of this test has also been developed by Chicot *et al.* [64] as discussed earlier.

Figure 4-16 shows a few typical SEM images containing the indentation at interfaces using a load of 50g, 100g and 200g. It is interesting to see that no crack was generated at the interface between the coating and the substrate. This suggests a strong bonding achieved between the YSZ coating and 430 porous stainless steel substrate in the present SPS process. However, the cracks were observed within the coating. This indicates that cohesive failure occurred in the coating before adhesive failure. Therefore, the adhesive strength of the coating-substrate interface was higher than the cohesive strength of the coating. The cohesive strength of the coating was indicated by the fracture toughness of the coating, measured above to be $1.61 \text{ MPa m}^{1/2}$ in the present coating condition. As a result, the interface fracture toughness of the coating-substrate interface would be $>1.61 \text{ MPa m}^{1/2}$.

The interface fracture toughness could be related to the substrate surface roughness before spraying. The higher the surface roughness, the higher the critical load, the better level of adhesion [101]. Therefore, the observed higher adhesive strength was due to the high surface

roughness of porous stainless steel substrate, which resulted from the mechanical interlocking of spray coating into the pores of stainless steel substrate.

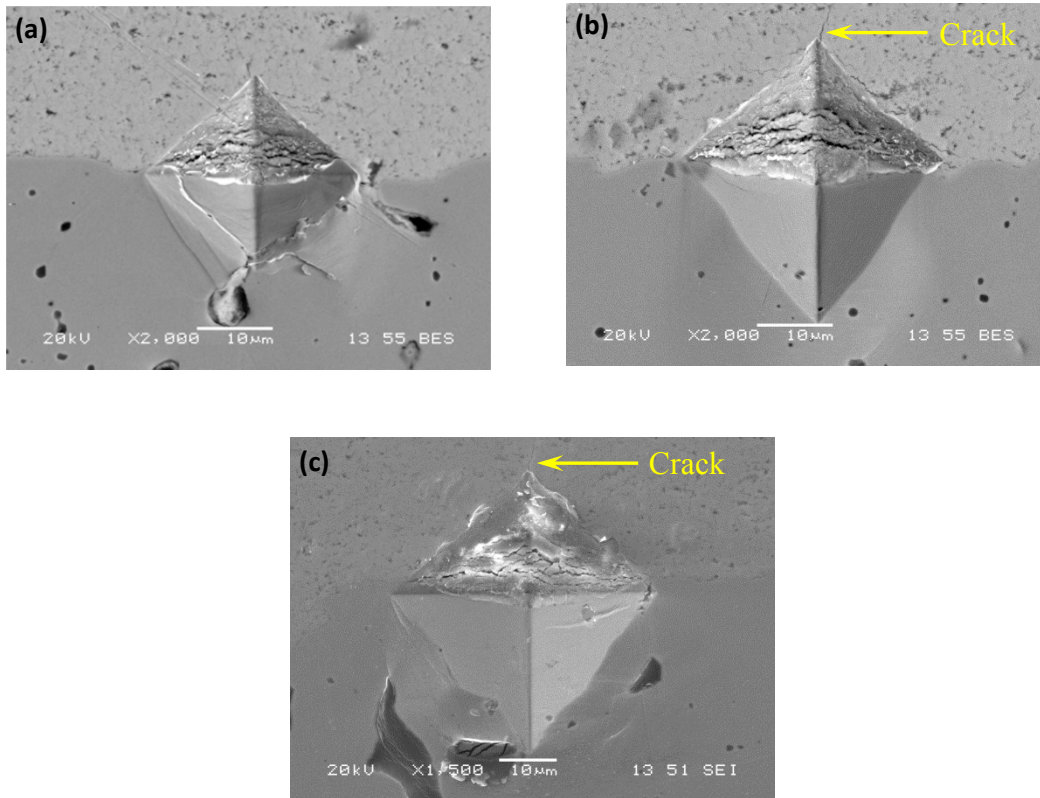


Fig. 4-16: Typical SEM images showing the indentation at interface of YSZ coatings deposited on 430 porous stainless steel substrate at a load of (a) 50 g, (b) 100 g, and (c) 200 g.

Chapter 5: Conclusions and Future Work

A summary of major results and contributions generated from this thesis work is presented in the following section, which is followed by recommendations for the future work.

5.1 Conclusions

This work has addressed the need for understanding material microstructure, residual stress and properties in the development of metal-supported SOFCs. Much of the focus of this work was on characterizing the residual stresses of suspension plasma sprayed YSZ electrolyte for metal-supported SOFCs. The major conclusions of this work are highlighted below.

1. The phase identification of coating revealed that the crystalline phase of suspension plasma sprayed 8 mol% YSZ was cubic, which delivered the highest conductivity. The comparison with powder sample indicated that the phase and the composition remained unchanged during the suspension plasma spraying process. The suspension plasma spraying process showed a potential for grain refinement and therefore, producing a fine and dense electrolyte layer. A smaller grain size could improve the flatness of the sheets for use in SOFC stacks, and the mechanical properties, thereby the performance of the coating.
2. The residual stress at room temperature was determined to be approximately 90 MPa in tension for the YSZ electrolyte coating made with a spray condition consisting of a torch power of 133 kW and a stand-off distance of 90 mm on LSM/YSZ + MG 0.2 substrate. This

suggests that the quenching stress was larger than the thermal mismatch stress. This result was likely due to the fairly small differences between the CTEs of the three component layers.

3. The observed microstructural features, such as porosity, microcracks and segmentation cracks relaxed the residual stresses formed in the cooling phase after plasma deposition. Therefore, the measured residual stresses at room temperature were the remaining stresses in the YSZ electrolyte, which included the stress-relieving effect of the segmentation cracks.
4. The residual stress decreased gradually to about 39 MPa when the temperature increased stepwise from room temperature to 750°C. The decrease of the residual stress with increasing temperature was a consequence of the combined changes in the Young's modulus, thermal expansion mismatch and generation of new micro-defects, as well as the possible creep deformation in the porous stainless steel substrate.
5. Of the deposition conditions studied, the coating made with a torch power of 133 kW and a stand-off distance of 90 mm exhibited the highest residual stress. This was due to the formation of a relatively dense microstructure without excessive cracking. The lower level of residual stresses at a lower torch power or longer stand-off distance was attributed to the presence of a higher amount of porosity and weaker inter-splat adhesion in the coatings. In contrast, the lower level of residual stresses at a higher torch power or shorter stand-off distance was due to a stress-relieving effect of more cracks arising from a faster cooling rate

after plasma spraying caused by the high heat input and the resulting higher temperature gradient.

6. The trends of change in the residual stress with the torch power and stand-off distance were similar for both LSM/YSZ + MG 2 and MG 0.2 substrates. However, the magnitude of residual stresses in the coatings deposited on MG 0.2 substrates at a lower torch power or longer stand-off distance and higher torch power or shorter stand-off distance was slightly higher than that in the coatings on LSM/YSZ + MG 2 substrate. Unlike LSM/YSZ + MG 2, the coating deposited on MG 0.2 substrate at a lower torch power and longer stand-off distance did not show the formation of segmentation cracks and therefore, resulted in a higher residual stress. Furthermore, at a higher torch power and shorter stand-off distance on MG 0.2, segmentation cracks did not penetrate all the coating thickness and therefore, they appeared to be less severe than those in the LSM/YSZ + MG 2. Therefore, the residual stresses were higher in these conditions on the MG 0.2 substrate.
7. Micro-hardness of the coatings increased with increasing torch power or decreasing stand-off distance. With increasing torch power or decreasing stand-off distance, porosity in the coating reduced, which led to an increase in the micro-hardness. The highest hardness was observed with a torch power of 162 kW and a stand-off distance of 90 mm owing to its lowest porosity, while the lowest hardness was observed with a torch power of 100 kW and a stand-off distance of 90 mm in condition G4 due to its highest porosity.

8. Fracture toughness of the coating with a torch power of 133 kW and a stand-off distance of 90 mm was $1.61 \text{ MPa m}^{1/2}$ measured using indentation technique. This was in agreement with that reported for tap cast 8mol% YSZ ($1.65 \text{ MPa m}^{1/2}$).
9. The interface indentation test revealed that the adhesion strength of coating to the substrate was higher than the cohesive strength of the coating. Therefore, interface fracture toughness was greater than the fracture toughness of the coating.

5.2 Major contributions

As discussed earlier, a metal-supported SOFC structure may fail by a variety of mechanisms, driven in-part by large tensile residual stresses quantified for YSZ in this thesis. Generally speaking, a large tensile residual stress will cause cracking as observed in the present study. These stresses also increase likelihood of decohesive or delamination failures. Thus, one may use the results of this work to determine an appropriate set of deposition conditions necessary to produce released structures under intermediate levels of stress. Specifically, reducing the level of net tensile stress and thereby reducing segmentation cracking could be achieved by depositing electrolyte on an electrode with a higher thermal conductivity or by reducing the plasma heat impulse with each torch pass. Moreover, this work provides an important input for understanding other mechanical properties such as flexural strength as it is required to know the residual stresses in order to accurately characterize these mechanical properties.

This work also illustrates the high temperature behavior of residual stresses in a metal-supported SOFCs for the first time. This provides an important insight into understanding the failure mechanisms at typical SOFC operating temperatures. In addition, it enables us to accurately characterize various mechanical properties at SOFC typical operating temperatures using high temperature residual stresses.

5.3 Recommendations for the future work

This work represents progress in an important material and mechanical aspects of metal-supported SOFCs development. However, these results lead to several additional questions and areas for continued investigations. Those questions and areas are presented below.

1. The as-deposited residual stress state should be characterized over a wider range of processing conditions. For example, various other combinations of torch powers and stand-off distances can be analyzed to check systematically their effects on the microstructure and residual stresses of the coating.
2. Characterization of variables with additional processing parameters such as plasma gas flow rate, nozzle size, and substrate temperature should be undertaken to develop a greater understanding of residual stress management.

3. The electrolyte thickness in the present study is about 45-50 μm . Studies can be conducted to investigate the microstructure and residual stress of electrolyte having a smaller thickness as is required to achieve lower electrolyte resistance.
4. In order to firmly establish reasons for the decrease in the residual stress with increasing temperature, cycling test is required followed by permeability measurements to identify a generation of new defects in the coating which relax residual stress at higher temperatures. Also, creep tests would be helpful to ascertain the presence of the creep in porous stainless steel substrate and quantify the stress relaxation due to creep.
5. Further studies are required to reduce the tensile residual stress and thereby the segmentation cracking using different material and processing conditions.
6. Young's modulus was considered constant during the study on the effect of process parameters on the residual stress. However, Young's modulus of the coating may change with the change in the process parameters and therefore, its characterization and variation with various spray parameters should be considered to better understand the residual stress variation with various process parameters.
7. The variation of fracture toughness with different torch powers and stand-off distances needs to be studied.

8. A new method needs to be explored to quantify the interface adhesion strength of the YSZ electrolyte layer. In addition, the interface adhesion strength of electrolyte to a cathode layer should also be studied.

This thesis provides important insight into the materials issues related to the development of structurally viable metal-supported SOFCs. These contributions, as well as the completion of the additional work identified above will help to lead to the further development and potentially widespread use of metal-supported SOFCs.

REFERENCES

- [1]. Energy Information Administration, International Energy Outlook, DOE/EIA-0484 (2009).
- [2]. S.M. Haile, "Fuel cell materials and components", *Acta Materialia*, 51(19) (2003) pp. 5981-6000.
- [3]. S.C. Singhal, "Advances in solid oxide fuel cell technology", *Solid State Ionics*, 135(1) (2000) pp. 305-313.
- [4]. J. Murray and D. King, "Climate policy: Oil's tipping point has passed", *Nature*, 481 (2012) pp. 433-435.
- [5]. D.A. Howey, "A challenging future for cars", *Nature Climate Change*, 2 (2012) pp. 28-29.
- [6]. T. Suzuki, Z. Hasan, Y. Funahashi, T. Yamaguchi, Y. Fujishiro and M. Awano, "Impact of anode microstructure on solid oxide fuel cells" *Science*, 325 (2009) pp. 852-855.
- [7]. Y.H. Huang, R.I. Dass, Z.L. Xing and J.B. Goodenough, "Fuel Cell", *Science*, 308 (2005) pp. 844-847.
- [8]. C.K. Dyer, "Fuel cells for portable applications" *J. Power Sources* 106 (2002) pp. 31-34.
- [9]. B. Sorensen, "Hydrogen and fuel cells: emerging technologies and application", Amsterdam, Elsevier academic press, 2005.
- [10]. S. Singhal and K. Kendall, "High temperature solid oxide fuel cells: fundamentals, design and applications", New York, Elsevier, 2003.
- [11]. L. Rose, O. Kesler, C. Decès-Petit, T. Troczynski and R. Maric, "Characterization of porous stainless steel 430 for low- and intermediate-temperature solid oxide fuel cell (SOFC) substrates" *Inter. J. Green Energy*, 6 (2009) pp. 638-645.
- [12]. W.N. Liu, X. Sun and M.A. Khaleel, "Effect of creep of ferritic interconnect on long-term performance of solid oxide fuel cell stacks" *Fuel Cells* 10, 4 (2010) pp. 703-717.

- [13]. P. Lamp, J. Tachtler, O. Finkenwirth, S. Mukerjee and S. Shaffer, “Development of an auxiliary power unit with solid oxide fuel cells for automotive applications” *Fuel Cells* 3, (2003) pp. 1-7.
- [14]. B.C.H. Steele, “Material science and engineering: The enabling technology for the commercialisation of fuel cell systems”, *J. Mat. Sci.*, 36 (2001) pp. 1053-1068.
- [15]. B.C.H. Steele and A. Heinzl, “Materials for fuel-cell technologies,” *Nature*, 414 (2001) pp. 345-352.
- [16]. B.C.H. Steele, “Materials for high-temperature fuel cells,” *Philosophical Transactions: Mathematical, Phys. and Eng. Sci.*, 354(1996) pp. 1695-1710.
- [17]. D. Waldbillig and O. Kesler, “Characterization of metal-supported axial injection plasma sprayed solid oxide fuel cells with aqueous suspension plasma sprayed electrolyte layers”, *J. Power Source*, 191 (2009) pp. 320-329.
- [18]. R. Hui, J. Berghaus, C. Decès-Petit, W. Qu, S. Yick, J. Legoux and C. Moreau, “High performance metal-supported solid oxide fuel cells fabricated by thermal spray” *J. Power Sources*, 191 (2009) pp. 371-376.
- [19]. Q. Huang, J. Berghaus, D. Yang, S. Yick, Z. Wang, B. Wang and R. Hui, “Polarization analysis for metal-supported SOFCs from different fabrication processes” *J. Power Sources*, 177 (2008) pp. 339-347.
- [20]. E.D. Wachsman and K.T. Lee, “Lowering the temperature of solid oxide fuel cells” *Science*, 334 (2011) pp. 935-939.
- [21]. Z. Shao and S.M. Haile, “A high-performance cathode for the next generation of solid-oxide fuel cells” *Nature*, 431 (2004) pp. 170-173.

- [22]. M. Brandner, M. Bram, J. Froitzheim, H.P. Buchkremer and D. Stöver, “Electrically conductive diffusion barrier layers for metal-supported SOFC” *Solid State Ionics*, 179 (2008) pp. 1501-1504.
- [23]. J. Matejicek, S. Sampath, P.C. Brand and H.J. Prask, “Quenching, thermal and residual stress in plasma sprayed deposits: NiCrAlY and YSZ coatings”, *Acta Mater.*, 47 (1999) pp. 607-617.
- [24]. R. McPherson, “Review of microstructure and properties of plasma sprayed ceramic coatings” *Surf. Coat. Technol.*, 39-40 (1989) pp. 173-181.
- [25]. D. Waldbillig and O. Kesler, “Effect of suspension plasma spraying processing parameters on YSZ coating microstructure and permeability”, *Surf. Coat. Tech.*, 205(23-24) (2011) pp. 5483-5492.
- [26]. W. Fischer, J. Malzbender, G. Blass and R.W. Steinbrech, “Residual stresses in planar solid oxide fuel cells” *J. Power Sources*, 150 (2005) pp. 73-77.
- [27]. J. Malzbender, W. Fischer and R.W. Steinbrech, “Studies of residual stresses in planar solid oxide fuel cells” *J. Power Sources*, 182 (2008) pp. 594-598.
- [28]. K. Huang and H.D. Harter, “Temperature-dependent residual stresses in plasma sprayed electrolyte thin-film on the cathode substrate of a solid oxide fuel cell” *Solid State Ionics*, 181 (2010) pp. 943-946.
- [29]. A.B. Stambouli and E. Traversa, “Solid oxide fuel cells (SOFCs): a review of an environmentally clean and efficient source of energy”, *Renewable and Sustainable Energy Reviews*, 6 (2002) pp. 433-455.
- [30]. E. Baur and H.Z. Preis, “Fuel-gas cells with solid electrolytes” *Electrochem*, 43 (1937) pp. 727-732.

- [31]. N.Q. Minh, "Ceramic Fuel Cells" *J.Am.Ceram.Soc.*, 76(1993) pp. 563-588.
- [32]. N.Q. Minh and T. Takahashi, *Science and Technology of Ceramic Fuel Cells*, Elsevier, Amsterdam, The Netherlands, 1995.
- [33]. J.J.P Hujismans, "Ceramics in solid oxide fuel cells", *Current Opinion in Solid State and Materials Science*, 5(4) (2001) pp. 317-323.
- [34]. O. Yamamoto, Y. Arati, Y. Takeda, N. Imanishi, Y. Mizutani, M. Kawai and Y. Nakamura, "Electrical conductivity of stabilized zirconia with ytterbia and Scandia" *Solid State Ionics*, 79 (1995) pp. 137-142.
- [35]. K. Han, Y. Jeong, H. Lee and C. Kim, "Fabrication of NiO/YSZ anode material for SOFC via mixed NiO precursors" *Materials Letters*, 61 (2007) pp. 1242-1245.
- [36]. P. Fauchais, "Understanding plasma spraying", *J. of Phys. D: Appl. Sci.*, 37 (2004) pp. 86-108.
- [37]. M. Moss, D.L. Smith and R.A. Lefever, "Metastable phases and superconductors produced by plasma-jet spraying" *Appl. Phys. Lett.*, 5 (6) (1964) pp. 120-121.
- [38]. P. Fauchais, J.F. Coudert, M. Vardelle, A. Vardelle and A. Denoirjean, "Diagnostics of thermal spraying plasma jets", *J. Therm. Spray Technol.* 1(2) (1992) pp. 117-128.
- [39]. J.F. Coudert, M.P. Planche and P. Fauchais, "Velocity measurements of DC plasma jets based on arc root fluctuations", *Plasma Chem. Plasma Process*, 15(1) (1995) pp. 47-70.
- [40]. S.C. Snyder, L.D. Reynolds, J.R. Fincke, G.D. Lassahn, J.D. Grandy and T.E. Repetti, "Electron-temperature and electron-density profiles in an atmospheric-pressure argon plasma jet", *Phys. Rev. E: Stat. Phys. Plasmas Fluids Relat. Interdisc. Topics*, 50(1) (1994) pp. 519-525.

- [41]. J. Cedelle, M. Vardelle and P. Fauchais, "Influence of stainless steel substrate preheating on surface topography and on millimeter and micrometer sized splat formation", *Surf. Coat. Technol.*, 201 (2006) pp. 1373-1382.
- [42]. H. Bhat and H. Hermann, Proc. of the International Conference on Metallurg. Coat. Proc. Technol., San Diego, CA, USA, April 5-8, (1982) pp. 227-234.
- [43]. O. Marchand, L. Girardot, M.P. Planche, P. Bertrand, Y. Bailly and G. Bertrand, "An insight into suspension plasma spray: injection of the suspension and its interaction with the plasma flow", *J. Thermal Spray Technol.*, 20(6) (2011) pp. 1310-1320.
- [44]. O. Arevalo-Quintero, D. Waldbillig and O. Kesler, "An investigation of the dispersion of YSZ, SDC, and mixtures of YSZ/SDC powders in aqueous suspensions for application in suspension plasma spraying", *Surf. Coat. Tech.*, 205(1-2) (2011) pp. 5218-5227.
- [45]. J. Karthikeyan, C.C. Berndt, J. Tikkanen, S. Reddy and H. Herman, "Plasma spray synthesis of nanomaterial powders and deposits" *Mater. Sci. Eng. A*, 238 (1997) pp. 275-286.
- [46]. Y. Mizoguchi, M. Kagawa, M. Suzuki, Y. Syono and T. Hirai, "Synthesis of ultrafine particles and thin films of BaFe₁₂O₁₉ by the spray-ICP technique", *Nanostruct. Mater.*, 4 (5) (1994) pp. 591-596.
- [47]. R. Hui, Z. Wang, O. Kesler, L. Rose, J. Jankovic, S. Yick, R. Maric and D. Ghosh, "Thermal plasma spraying of SOFCs: applications, potential advantages, and challenges" *J. of Power Sources*, 170 (2) (2007) pp. 308-323.
- [48] R.B. Heimann, "Plasma-spray coating", John Wiley & Sons, pp. 19, 2008.

- [49]. S. Kuroda, T. Dendo and S. Kitahara, "Quenching stress in plasma sprayed coatings and its correlation with deposit microstructure", *J. of Thermal Spray Techno.*, 4(1) (1995) pp. 75-84.
- [50]. B.D. White, O. Kesler and L. Rose, "Air Plasma Spray Processing and Electrochemical Characterization of SOFC Composite Cathodes" *J. of Power Sources*, 178 (1) (2008) pp. 334-343.
- [51]. O. Kesler, J. Matejcek, S. Sampath, S. Suresh, T. Gnaeupel-Herold, P.C. Brand and H.J. Prask, "Measurement of residual stress in plasma-sprayed metallic, ceramic and composite coatings", *Mater. Sci. Eng. A*, 257 (1998) pp. 215-224.
- [52]. J. Matejcek and S. Sampath, "Intrinsic residual stresses in single splats produced by thermal spray processes", *Acta Materialia*, 49(11) (2001) pp. 1993-1999.
- [53]. C. Godoy, E.A. Souza, M.M. Lima and J.C.A. Batista, "Correlation between residual stresses and adhesion of plasma sprayed coatings: effects of a post-annealing treatment", *Thin Solid Films*, 420 -421 (2002) pp. 438-445.
- [54]. B.B. He, Two Dimensional X-Ray Diffraction, John Wiley & Sons, Inc., 19, 2009.
- [55]. G.M. Pharr, "Measurement of mechanical properties by ultra-low load indentation", *Mater. Sci. Eng. A*, 253 (1-2) (1998) pp. 151-159.
- [56]. ASTM1421-99, ASTM C 1421-99 Standard Test Methods 15.01, 1999.
- [57]. ASTM E-399, American Society for Testing and Materials, 1987.
- [58]. S. Zhang and X. Zhang, "Toughness evaluation of hard coatings and thin films", *Thin Solid Films*, 520 (2012) pp. 2375-2389.

- [59]. G.R. Anstis, P. Chantikul, B.R. Lawn and D.B. Marshall, "A critical evaluation of indentation techniques for measuring fractures toughness" *J. Am. Ceram. Soc.*, 64 (9) (1981) pp. 533-538.
- [60]. C.C. Berndt, "Instrumented tensile adhesion tests on plasma sprayed thermal barrier coatings", *J. Mater. Eng.*, 11(4) (1989) pp. 275-282.
- [61]. A. Tronche and P. Fauchais, "Hard coatings (Cr203, WC-Co) properties on aluminium or steel substrates" *Mat. Sci. Eng.*, 92 (1987) pp. 133-144.
- [62]. J. Lesage and D. Chicot, "Role of residual stresses on interface toughness of thermally sprayed coatings", *Thin Solid Films*, 415 (2002) pp. 143-150.
- [63]. H. Yakabe, Y. Baba, T. Sakurai and Y. Yoshitaka, "Evaluation of the residual stress for anode-supported SOFCs", *J. Power Sources*, 135 (2004) pp. 9-16.
- [64]. P.S. Prevéy, *Metals Handbook*, Vol.10, Metals Park, ASM (1986) pp. 380-392.
- [65]. W. Fischer, H. Gruhn and W. Mallèner, "Residual stress in plasma-sprayed ceramic coatings", *Mat. Sci. Forum.*, 228-231 (1996) pp. 481-486.
- [66]. S.P.S. Badwal and F.T. Ciacchi, "Oxygen-ion conducting electrolyte materials for solid oxide fuel cells" *Ionic*, 6 (2000) pp. 1-21.
- [67]. W. Xia, Y. Yang, H. Zhang and G. Wang, "Fabrication and electrochemical performance of solid oxide fuel cell components by atmospheric and suspension plasma spray", *Trans. Nonferrous Met. Soc. China*, 19(2009) pp. 1539-1544.
- [68]. O. Bellon, R. Ratnaraj and D. Rodrigo, "10YSZ based electrolyte materials for electrolyte supported SOFCs" *5th European SOFC forum Proc.*, 1 (2002) pp. 184-190.

- [69]. S. Molin, B. Kusz, M. Gazda and P. Jasinski, "Evaluation of porous 430L stainless steel for SOFC operation at intermediate temperatures", *J. Power Sources*, 181 (2008) pp. 31-37.
- [70]. A. Atkinson and B. Sun, "Residual stress and thermal cycling of planar solid oxide fuel cells", *Mater. Sci. Technol.*, 23 (2007) pp. 1137-1143.
- [71]. D. Cui and M. Cheng, "Thermal stress modeling of anode supported micro-tubular solid oxide fuel cell", *J. Power Sources*, 192(2) (2009) pp. 400-407.
- [72]. I.R. Gibson, G.P. Dransfield and J.T.S. Irvine, "Sinterability of commercial 8 mol% yttria-stabilized zirconia powders and the effect of sintered density on the ionic conductivity", *J. Mater. Sci.* 33 (1998) pp. 4297-4305.
- [73]. J. Ilavsky and J.K. Stalick, "Phase composition and its changes during annealing of plasma-sprayed YSZ", *Surf. Coat. Technol.*, 127 (2000) pp. 120-129.
- [74]. H. Yakabe, Y. Baba, T. Sakurai, M. Satoh, I. Hirosawa and Y. Yoda, "Evaluation of residual stresses in a SOFC stack", *J. Power Sources*, 131 (2004) pp. 278-284.
- [75]. G. Sattonnay, M. Lahrichi, M. Herbst-Ghysel, F. Garrido and L. Thomè, "Stress field induced by swift heavy ion irradiation in cubic yttria stabilized zirconia", *J. Appl. Physics*, 101 (2007) 103516 pp. 1-6.
- [76]. X.C. Zhang, B.S. Xu, F.Z. Xuan, S.T. Tu, H.D. Wang and Y.X. Wu, "Porosity and effective mechanical properties of plasma-sprayed Ni-based alloy coatings", *Appl. Surf. Sci.*, 255 (2009) pp. 4362-4371.
- [77]. S. Kozerski, L. Latka, L. Pawlowski, F. Cernuschi, F. Petit, C. Pierlot, H. Podlesak and J.P. Laval, "Preliminary study on suspension plasma sprayed ZrO₂+ 8wt.% Y₂O₃ coatings", *J. Eur. Ceram. Soc.*, 31(12) (2011) pp. 2089-2098.

- [78]. R. Vaßen, H. Kaßner, G. Mauer and D. Stöver, “Suspension plasma spraying: process development and applications”, Proc. of the International Thermal Spray Conference, ASM International, May 4-7, 2009 (Las Vegas, NV), pp. 162-167.
- [79]. H. Kassner, R. Siegert, D. Hathiramani, R. Vassen and D. Stoever, “Application of suspension plasma spraying (SPS) for manufacture of ceramic coatings”, *J. Thermal Spray Technol.*, 17(1) (2008), pp. 115-123.
- [80]. S. Giraud and J. Canel, “Young’s modulus of some SOFCs materials as a function of temperature”, *J. Euro. Ceram. Soc.*, 28 (2008) pp. 77-83.
- [81]. T. Kushia, K. Satob, A. Unemotob, S. Hashimotoa, K. Amezawaa and T. Kawadaa, “Elastic modulus and internal friction of SOFC electrolytes at high temperatures under controlled atmospheres”, *J. Power Sources*, 196 (19) (2011) pp. 7989-7993.
- [82]. B.C. Church, T.H. Sanders, R.F. Speyer, J.K. Cochran, “Thermal expansion matching and oxidation resistance of Fe–Ni–Cr interconnect alloys”, *Mater. Sci. Eng. A*, 452-453 (2007) pp. 334-340.
- [83]. C.C. Berndt, “Failure processes within ceramic coatings at high temperatures”, *J. Mater. Sci.*, 24 (1989) pp. 3511-3520.
- [84]. E. Klar and P. Samal, Powder Metallurgy Stainless Steels, ASM International, 2007.
- [85]. J. Kondoh, H. Shiota, K. Kawachi and T. Nakatani, “Yttria concentration dependence of tensile strength in yttria-stabilized zirconia”, *J. Alloys and Compounds*, 365 (2004) pp. 253-258.
- [86]. Y. Wang, J.G. Legoux, R. Neagu, S. Hui and B.R. Marple, “Suspension plasma spray and performance characterization of half cells with NiO/YSZ anode and YSZ electrolyte”, *J. Therm. Spray Technol.*, 21(1) (2012) pp. 7-15.

- [87]. M. Marr and O. Kesler, "Permeability and microstructure of suspension plasma sprayed YSZ electrolytes for SOFCs on various substrates", *J. of Thermal Spray Technol.*, 2012.
- [88]. M. Friis, C. Persson and J. Wigren, "Influence of particle in-flight characteristics on the microstructure of atmospheric plasma sprayed yttria stabilized ZrO₂", *Surf. Coat. Technol.* 141(2-3) (2001) pp. 115-127.
- [89]. H.B. Guo, R. Vaßen and D. Stöver, "Atmospheric plasma sprayed thick thermal barrier coatings with high segmentation crack density", *Surf. Coat. Tech.*, 186(3) (2004) pp. 353-363.
- [90]. S.A. Sadeghi-Fadaki, K. Zangeneh-Madar and Z. Valefi, "The adhesion strength and indentation toughness of plasma-sprayed yttria stabilized zirconia coatings", *Surf. & Coat. Technol.*, 204 (2010) pp. 2136-2141.
- [91]. A. Bacciochini, J. Ilavsky, G. Montavon, A. Denoirjean, F. Ben-ettouil, S. Valette, P. Fauchais and K. Wittmann-tenezec, "Quantification of void network architectures of suspension plasma-sprayed (SPS) yttria-stabilized zirconia (YSZ) coatings using Ultra-small-angle X-ray scattering (USAXS)" *Mater. Sci. Eng. A*, 528 (2010) pp. 91-102.
- [92]. K. VanEvery, M.J.M. Krane and R.W. Trice, "Parametric study of suspension plasma-spray processing parameters on coating microstructures manufactured from nanoscale yttria-stabilized zirconia", *Surf. & Coat. Technol.*, 206 (2012) pp. 2464-2473.
- [93]. E. Meillot, R. Vert, C. Caruyer, D. Damiani and M. Vardelle, "Manufacturing nanostructured YSZ coatings by suspension plasma spraying (SPS): Effect of injection parameters", *J. Phys. D: Appl. Phys.*, 44 (2011) 194008 pp. 1-8.

- [94]. R. Chaim and M. Hefetz, "Effect of grain size on elastic modulus and hardness of nanocrystalline ZrO₂-3 wt% Y₂O₃ ceramic" *J. of Mater. Sci.*, 39 (2004) pp. 3057-3061.
- [95]. J.J. Kruzic and R.O. Ritchie, "Determining the toughness of ceramics from Vickers indentations using the crack-opening displacements: An experimental study", *J. Am. Ceram. Soc.*, 86 (8) (2003) pp. 1433-1436.
- [96]. Q. Chang, D.L. Chen, H.Q. Ru and C.P. Zhang, "Toughening mechanisms in iron-containing hydroxyapatite/titanium composites", *Biomaterials*, 31 (2010) pp. 1493-1501.
- [97]. X.J. Zhaoa, N. Zhang, H.Q. Rua, B. Liang and D.L. Chen, "Mechanical properties and toughening mechanisms of silicon carbide nano-particulate reinforced Alon composites", *Mater. Sci. and Eng. A*, 538 (2012) pp. 118-124.
- [98]. M. Radovic, E. Lara-Curzio, R. Trejo, B. Armstrong, and C. Walls, "Elastic properties, equibiaxial strength and fracture toughness of 8mol% YSZ electrolyte material for solid oxide fuel cells (SOFCs)", *Ceram. Eng. and Sci. Proc.*, 25 (3) (2004) pp. 287-292.
- [99]. Y. Liu, T. Nakamura, V. Srinivasan, A. Vaidya, A. Gouldstone and S. Sampath, "Non-linear elastic properties of plasma-sprayed zirconia coatings and associated relationships with processing conditions", *Acta Mater*, 55 (2007) pp. 4667-4678.
- [100]. Z. Marcano, J. Lesage, D. Chicot, G. Mesmacque, E.S. Puchi-Cabrera and N.M. Staia, "Microstructure and adhesion of Cr₃C₂-NiCr vacuum plasma sprayed coatings", *Surf. Coat. Technol.*, 202 (2008) pp. 4406-4410.
- [101]. G. Bourse, W. Xu, A. Mouftiez, L. Vandevoorde and M. Ourak, "Interfacial adhesion characterization of plasma coatings by V(z) inversion technique and comparison to interfacial indentation", *NDT&E International*, 45 (2012) pp. 22-31.

APPENDIX

LIST OF PUBLICATIONS (over past 12 months of my MAsC study)

A. Refereed journal papers (accepted or under review):

- 1) **A. Macwan**, D.L. Chen, M. Marr and O. Kesler, “Residual stresses in suspension plasma sprayed electrolytes in metal-supported SOFC half cells”, *Journal of Power Sources*, in press, Available online on August 24, 2012.
- 2) **A. Macwan**, D.L. Chen, M. Marr and O. Kesler “Effects of torch power and stand-off distance on microstructure and residual stress of suspension plasma sprayed YSZ coating” , (under internal review).

B. Conference Presentation:

- 1) **A. Macwan**, D.L. Chen, M. Marr and O. Kesler, “Evaluation of residual stress in suspension plasma sprayed electrolyte in metal-supported SOFCs”, The 24th Canadian Material Science Conference (CMSC), London, ON, June 5-8, 2012 (Oral presentation).